

**Systems approach based solution to fundamental limitations in unraveling spatial
and temporal regimes in nano-interrogation and nano-positioning**

by

Tathagata De

A dissertation submitted to the graduate faculty
in partial fulfillment of the requirements for the degree of

DOCTOR OF PHILOSOPHY

Major: Electrical Engineering

Program of Study Committee:
Murti V. Salapaka, Major Professor
Wolfgang Kliemann
Degang Chen
Umesh Vaidya
Zhengdao Wang
Saju Nettikadan

Iowa State University

Ames, Iowa

2008

Copyright © Tathagata De, 2008. All rights reserved.

UMI Number: 3316175

INFORMATION TO USERS

The quality of this reproduction is dependent upon the quality of the copy submitted. Broken or indistinct print, colored or poor quality illustrations and photographs, print bleed-through, substandard margins, and improper alignment can adversely affect reproduction.

In the unlikely event that the author did not send a complete manuscript and there are missing pages, these will be noted. Also, if unauthorized copyright material had to be removed, a note will indicate the deletion.



UMI Microform 3316175
Copyright 2008 by ProQuest LLC
All rights reserved. This microform edition is protected against
unauthorized copying under Title 17, United States Code.

ProQuest LLC
789 East Eisenhower Parkway
P.O. Box 1346
Ann Arbor, MI 48106-1346

dedicated to my ε -neighborhood:

Baba, Maa, Tithi

aar

Mou

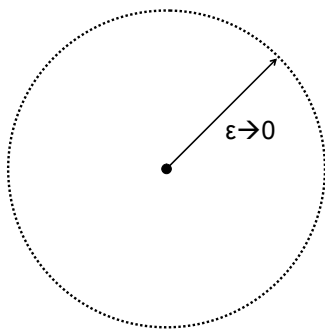


TABLE OF CONTENTS

LIST OF FIGURES	v
ACKNOWLEDGMENTS	xii
ABSTRACT	xvi
CHAPTER 1. INTRODUCTION	1
CHAPTER 2. SYSTEMS SOLUTION TO FUNDAMENTAL LIMITATION ON IMAGING BANDWIDTH IN CONTACT MODE PROFILE ESTI- MATION	7
2.1 Setup and Problem Formulation	8
2.2 Modeling tip-sample force as disturbance	9
2.3 Multi-objective controller design	10
2.4 Generalized version to estimate disturbance signal	11
2.5 A New Sample-Profile Signal	12
2.6 Controller design from H-infinity synthesis procedure	14
2.7 Zero error in disturbance (or profile) estimation for all bandwidth	14
2.8 Robustness of this signal to plant uncertainties	21
2.9 Effect of measurement noise in profile estimation	21
2.10 Observer Based Designs	23

2.11	Experimental Setup and Results	26
2.11.1	System identification	27
2.11.2	Control design, implementation and validation	28
2.11.3	Results	29
2.12	Conclusions	31
 CHAPTER 3. SYSTEMS SOLUTION TO FUNDAMENTAL LIMITATION		
IN IMAGE RELIABILITY IN INTERMITTENT MODE PROFILE ES-		
TIMATION		
3.1	Introduction	41
3.2	Source of spurious image	42
3.3	Experimental demonstration of sensor loss	44
3.4	Detection of probe loss	46
3.5	Cantilever dynamics and observer	46
3.6	Model mismatch	47
3.7	Conclusion	51
 CHAPTER 4. QUANTITATIVE STUDY OF YEAST MORPHOLOGY . .		
4.1	Role of AFM in cell wall characterization	54
4.1.1	Sample preparation for AFM	55
4.1.2	Study of cell morphology	56
4.2	Protocol for immobilization of live <i>Saccharomyces cerevisiae</i> cells for AFM imaging	57
4.2.1	Inoculation of yeast culture	57
4.2.2	Prepare immobilized cells for AFM imaging	58
4.3	Results and Discussion	59

4.3.1	Significance of quantitative imaging	61
4.3.2	Study of cell morphology	61
4.3.3	Inhibition of growth and roughness variation by Sodium Azide treatment	64
4.4	Conclusion:	64
CHAPTER 5. FUTURE WORK AND CONCLUSION		65
CHAPTER 6. AREAS OF PUBLICATIONS		69
BIBLIOGRAPHY		71

LIST OF FIGURES

Figure 1.1	A schematic of an AFM. A micro-cantilever is the main sensor that is soft enough to detect interatomic forces and has resonant frequency high enough to isolate other disturbances. The cantilever deflection is sensed by a laser incident on the back of the cantilever reflecting into a split-photodiode. The sample being interrogated is positioned using flexure stages that are actuated by piezo's. In contact mode operation, the photo-diode output is utilized by a feedback controller to maintain a constant deflection and the control signal gives the estimate of the sample profile. In tapping mode the cantilever is made to oscillate by the dither piezo and the changes to the periodic orbit due to tip-sample interactions give a measure of the sample profile.	2
Figure 2.1	AFM framework	33

Figure 2.2	Framework for the optimal control problem. The controller $K = [K_1 \ K_2]^T$ has two outputs - the control signal u with the objective of achieving robust set point regulation of the deflection signal y and high resolution through roll off of the transfer function from the setpoint r to the piezo response v ; and the signal \hat{d} with the objective of giving an accurate estimate of the sample profile \tilde{d} . Our design objective is to minimize weighted performance variable z_1 (weighted regulation error), z_2 (weighted noise sensitivity), z_3 (weighted control effort) and z_4 (weighted estimation error)	33
Figure 2.3	The schematic for the Robust \mathcal{H}_∞ framework with output and input multiplicative plant uncertainties.	34
Figure 2.4	(A) A schematic of the observer design - Gain matrices F and L need to be designed to achieve small profile estimation error, set point regulation and robustness with respect to class of plants (G, Δ) . (B) The form of (G, Δ) for input and output multiplicative uncertainties.	34
Figure 2.5	(A) Glover McFarlane Design: The controller K has two components - K_s designed exclusively for performance objective such as set point regulation, and K_r designed to achieve robustness of the loop. (B) The form of (G, Δ) . This uncertainty characterization is especially useful to characterize low damped pole uncertainties.	34

- Figure 2.6 (A) A schematic of MFP-3D. In this device the sample is kept on lateral scanner (XY positioning stage) which is a piezo actuated flexure stage. The motion in vertical direction is provided to the head which houses the cantilever and the detection system comprising of the laser and the photodiode. This motion is provided by the piezo actuated z -positioner. The photodiode output which measures the cantilever deflection is utilized by the control design to obtain set point regulation and to prescribe profile estimate signal. (B) A Schematic of control implementation on DSP. The deflection signal from photodiode is sampled at 5 MHz and is used by the control algorithm in the DSP. The control signal generated by the DSP is then amplified and fed into the Z-piezo. 35
- Figure 2.7 A comparison of experimentally (solid) obtained and fitted (dotted) frequency responses of the plant G 35
- Figure 2.8 Control Design: (A) Weighting function for Sensitivity, Complementary Sensitivity and Actuation signal (W_S, W_T and W_u) respectively (B) Transfer functions of controller K_1 and observer K_2 obtained from $hinf_{syn}$ design. 36
- Figure 2.9 Experimental validation: (A) and (B) The plot compares the simulated and the experimentally obtained sensitivity and complementary transfer functions respectively. There is a good match between the two. 36

Figure 2.10 (A) The experimental frequency response of the control effort u to sample topography illustrates that it is not a good estimate of topography at high frequencies (B) The experimental frequency response of the estimate \hat{d} to sample topography remains flat corroborating the analytical result that this transfer function is a constant - the magnitude plot is within ± 3 dB and the phase is near zero over the entire range. 37

Figure 2.11 (A) Experimental data shows that significantly superior images (left panel) are obtained by using the new imaging signal \hat{d} when compare to the existing use of the control effort u as the sample topography estimate. (B,C): The plots show that the u signal gives worse estimates as the frequency of the d is increased (150 Hz and 500 Hz). The magnitude plots are consistent but there is a considerable phase lag. The \hat{d} signal on the other hand has practically no phase lag. (D) Experimental data that shows that the new imaging signal \hat{d} follows a 1.4 KHz reference sine wave that the control signal is unable to track at all. . . . 38

- Figure 3.1 Steady state based imaging schemes can not differentiate between two different sample surfaces. As demonstrated in the figure, the AFM generates identical imaging signal for two different surfaces. In the left hand side, the cantilever is scanning a steep vertical surface. When the cantilever encounters the vertical wedge, due to high quality factor it takes typically $\frac{f_0}{Q}$ cycles to reach the steady state, where f_0 is the resonant frequency of the cantilever and Q is the quality factor. During this time, vertical scanner extends to reach the cantilever tip at a rate governed by the gain of the controller. Till it regains contact with the tip, actuation signal to the vertical scanner (u) does not represent the actual surface profile. This is evident from the schematic: where the surface reconstruction depending on the u signal creates a non-vertical wedge. On the other hand, when the surface is indeed a non-vertical one, the scanner could always keep the cantilever in contact with the surface, thereby creating a true reproduction of sample profile. 43
- Figure 3.2 Experimental demonstration of probe-loss: A square grating (dotted-line) is imaged in dynamic mode. As the cantilever comes of the surface, a spurious image (solid-line; a trapezoidal shape) is generated. 44
- Figure 3.3 Shows the experimentally obtained amplitude signal during ESM-AFM imaging. (a) and (b) shows the amplitude profile and reliability index when imaging a rectangular and triangular sample respectively. 45

Figure 3.4	Shows the experimental vertical piezo actuation signals during TM-AFM imaging. (a) and (b) shows the height profile based on vertical actuation signal when imaging a rectangular and triangular sample respectively.	46
Figure 3.5	Model of the cantilever near its resonant frequency is mimicked by a high speed (10 MHz) electrical circuit implemented on Xilinx Virtex II Pro XC2VPX30 FPGA. Non-zero value of e arises from initial condition mismatch, $\eta(t)$ and $h(p, \dot{p})$	48
Figure 3.6	In (a) and (b), a rectangular profile is imaged at 20 Hz and 1Hz respectively.	50
Figure 4.1	<i>Saccharomyces cerevisiae</i> in nutrient rich Media	60
Figure 4.2	Multiple <i>Saccharomyces cerevisiae</i> cells in nutrient rich media	60
Figure 4.3	Percent Change in Yeast height	62
Figure 4.4	Roughness variation in yeast cell wall	63
Figure 4.5	Height image of yeast cells without and without growth inhibitor: even though both cell cluster is layered on nutrient rich media, non-azide treated cell shows growth and roughness change but Azide treated yeast does not demonstrate any consistent pattern in growth or roughness change. Also, height image demonstrated Azide treated yeast is structurally intact after Azide treatment, hence the inactivity is contributed to Azide treatment only.	63

ACKNOWLEDGMENTS

My father always told me PhD is not my cup of tea. I believed him more and more every passing days. It took me six years to complete a task which many people finish in three to four years. The only reason I could keep going in this seemingly eternal journey is being surrounded by people who felt even more miserable than I did and shared their pain, grief and sorrows with me. Unlike other traditional acknowledgments, I am not going to say that continuing support of friends and neighbors helped me in achieving what I did. I would rather say, I was surrounded by people who felt that they are under a pile higher and deeper than me and that gave me strength to survive.

However, I must acknowledge people who got me in this soup. I was a happy employee at IBM Global Services and never planned to come to US. Unless they put me in mainframe projects, which for the first time in my life made me feel stupid and incapable of doing something, I would never come here. So here is the first catalyst for my PhD. Then the visa officer at Mumbai visa office has to share the blame: he could have rejected my visa because I did not have any GRE or TOEFLE score. Unfortunately, a glorifying letter from Dr. Salapaka made him believe that I am going to be the brightest student under sun and GRE is too small a test for me.

I can not blame Mrityunjay enough for his ever encouraging words to pursue PhD. I was happily ride-sharing with him in his yellow (ok, he painted it steel gray later) Bajaj Priya

scooter to IBM. But he convinced me that I should do better. I heeded his advise and got myself stuck in this.

Family

My mom (Ms Kajal De) sent my dad (Mr Manab Kumar De) to prevent me from coming to US. He has a convincing power which supersedes any politician. I told him, ‘If you say just once: Don’t go; I will not. I will never blame you and I will be happy here.’ He did not. Probably, I felt an obligation to him to go for a doctoral work because he left his almost complete PhD just for me: to raise me as a capable son. My mom’s eyes still moisten when she finds out his yellowed publications under the closet. No dad (*I know of*) has done what he did for me, the least I could do is to spend six years of my life to complete what he started.

My mom and my sister (Ms Sunrita De, Tithi) are the source of most stupid inspirations of my life: they are just too happy that their *Tathai* is doing PhD in USA. They take far more pride and glory in what I do everyday. I just could not let them down!

Apartment and Neighborhood

Once I came to Iowa State University, I was surrounded by a crowd of very enthusiastic group of grad students who were forever unhappy and convinced about a bleak future. I quickly appreciated that only way to survive is to draw a bleaker and darker future during discussion. Rajesh, Rakesh, Murli (1 and 2), Amit, Amrita, Vipul, Jahnavi and Sutti are to name a few in Preeti Seema Apartment who dined, whined and wineed with me in 2001.

I have become the grand old man of Iowa and too many people became my roommates and graduated before me. If I start counting: Biswajit, Kalyanjit, Siddhartha, Durga, Supriyo,

Abhinav and Debjy. The list seems endless. However, Supri and Debjy shared my pain and fed me four times a week during my last years of PhD, so I owe them special thanks. My good luck with roommates continued with Raj in Charlotte.

My neighboring apartment always produced great whiners. I must admire Shailesh and Sunil for their ever evolving source of grief and frustration. Specially Sunil supported me emotionally and intellectually during my last two years: we analyzed Stephen Colbert and Bill O'Reilly everyday on our porch and concluded we are smarter than most of the living beings which ever walked, ran or crawled on earth. Therefore we must be able to complete the PhD. Their another roommate Jaju was source of innovative money-saving ideas, including a fabulous scheme to enjoy Dish Network with all Indian channels at an affordable rate. That must have delayed PhD by six months.

Research team and Laboratory

Dr. Srinivasa Salapaka is the person whom I owe my confidence in experimentation and theory. While working with him in profile estimation, I gained confidence in instrumentation to a level, which was almost dangerous. He stood beside me for late nights when I debugged the instrument. I was the luckiest researcher in our group to have him, Abu and Anil as my mentor.

Dr. Murti Salapaka, my major professor, was more than an adviser. He thrived to make our lab a powerhouse of ideas and motivated people to deliver on the promises. I am confident that in absence of his constant desire to achieve higher goals, we could not come up with so many stellar results in last six years.

Deepak deserves a special mention: I can not count the ways he influenced my work. He

was the key person inviting me in this lab, we scored well (and bad) in tests and we debugged instruments together. He knows what he did for me: I do not want to elaborate anymore.

Three new entrants in our lab were source of unbeatable optimism: Hullas, Pranav and Tanuj kept the spirit high even during the most difficult days in our lab. It was just refreshing experience. Antony was another person behind the scene. He coped with my endless weird requests during my yeast experimentation.

Special Mention

Tithi has been my best pal in all these years. Both of us shared the pain of endless study material, even though none of us disclosed how little we studied. She has such a confidence on me that I just could not fail her. For last six years she shared my depressions and anxieties with judiciousness of an elder sister, even though she is seven years younger to me. I wish she will achieve more than what I did. She deserves it.

Last but not the least, this thesis would have taken at least one more year to complete if a new catalyst did not come into play. Ms Rajendrani Mukherjee (now, Mrs. De) kept me on my toes to complete my thesis. I could not keep my cool many times at the face of her persistence. But she never gave up and made me complete the second most challenging task in my life (first being to convince her to come to USA). I will not belittle her by thanking!

ABSTRACT

A design scheme that achieves an optimal tip-sample force regulation with an ideal topography image reconstruction is presented. It addresses the problem of obtaining accurate sample profiles when scanning at high bandwidth while maintaining a constant cantilever-tip sample force in atomic force microscopes. It is shown that the proposed scheme provides a faithful replica of the sample at all relevant scanning speeds limited only by the inaccuracy in the model for the atomic force microscope. This provides an improvement over existing designs where the sample profile reconstruction is typically bandwidth limited. The experimental results corroborate the theoretical development.

Conventional imaging signals such as the amplitude signal and the vertical piezoactuation signal cannot identify the areas of probe loss, where dynamic atomic force microscopy based image where the cantilever fails to be an effective probe of the sample. A real-time methodology is developed to determine regions of probe loss. It is experimentally demonstrated that probe-loss affected portion of the image can be unambiguously identified by a real-time signal called reliability index. Reliability index, apart from indicating the probe-loss affected regions, can be used to minimize probe-loss affected regions of the image, thus aiding high speed AFM applications.

A new immobilization technique for quantitative imaging and topographic characterization of living yeast cells in solid media using Atomic force microscope (AFM) is presented. Unlike

previous techniques, proposed technique allows almost complete cell surface to be exposed to environment and studied using AFM. Apart from the new immobilization protocol, in this report, for the first time, high resolution height imaging of live yeast cell surface in intermittent contact mode is presented. High resolution imaging and significant improvement in operational stability facilitated investigation of growth patterns and evolution of surface morphology in quantitative terms. Growth rate of mother cell and budding cell showed distinct patterns over the imaging time.

CHAPTER 1. INTRODUCTION

The Atomic Force Microscope (AFM), since its invention by Gerd Binnig and Christoph Gerber in 1985 [1], continues to have a significant impact on many areas of science and technology. The main operational idea of an AFM is to employ a relatively soft micro-cantilever with very high resonant frequency to sense the extremely small interactive forces between the tip and the sample. The small stiffness of micro-cantilever facilitates detection of inter-atomic forces whereas high resonant frequency reduces the effect of various extraneous sources of vibrations. The sample topography is imaged by displacements of micro-cantilever tip as the sample surface moves under it. An AFM consists of a micro-cantilever, a sample positioner typically piezo-actuated to provide fine nano-scale displacements to the sample, a detection system for measuring cantilever deflections, and a control system for maintaining a desired operating condition (see Figure 1.1). The AFM has enabled probing and manipulation of different physical variables that include magnetic, electrical, biological and chemical properties in atomic scales [2, 3]. This investigation includes a wide range of materials which includes thin and thick film coatings, ceramics, composites, glasses, synthetic and biological membranes, metals, polymers, and semiconductors. This device is used to study a variety of phenomena such as abrasion, adhesion, corrosion, etching, friction, lubrication, plating, and polishing [2, 4]. Consequently, AFM has revolutionized basic research in sciences such as in biology, chemistry, material science and tribology [3, 5, 6, 7, 8], and has greatly affected technologies

such as electronics, telecommunications, biological, chemical, nano-mechanical [9], and energy industries.

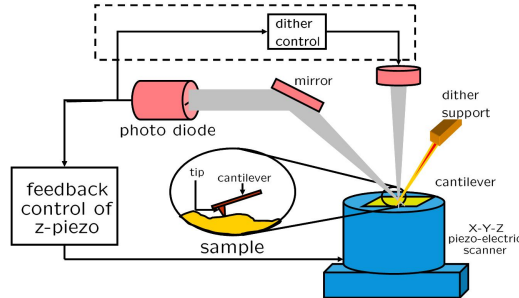


Figure 1.1 A schematic of an AFM. A micro-cantilever is the main sensor that is soft enough to detect interatomic forces and has resonant frequency high enough to isolate other disturbances. The cantilever deflection is sensed by a laser incident on the back of the cantilever reflecting into a split-photodiode. The sample being interrogated is positioned using flexure stages that are actuated by piezo's. In contact mode operation, the photo-diode output is utilized by a feedback controller to maintain a constant deflection and the control signal gives the estimate of the sample profile. In tapping mode the cantilever is made to oscillate by the dither piezo and the changes to the periodic orbit due to tip-sample interactions give a measure of the sample profile.

However, its considerable potential still needs to be tapped. There is still significant scope in improvement of these devices in achieving high resolution images at a high rate while maintaining its reliability in the sense of easy repeatability of experiments. In this context, the control design forms an important component toward achieving these goals. This has led to a growing interest in Atomic Force Microscopy in the systems community. Their contribution has been in analysis, modeling, and improving device performance. Concepts from dynamical systems have also been used in studying micro-cantilevers and analyzing their interactions with sample surfaces. System tools were used to study steady state behaviors of cantilevers [10, 11] explain rich complex behavior observed in experiments [12, 13], and derive fundamental

limitations on this technology [14]. The system identification techniques are used to provide mathematical models of the system without having the need to deal with the complex geometry or material composition of the device [15, 16, 17, 18, 19]. The fine resolution and large range of motion for these devices are typically provided by piezo-actuators. However, piezo-actuation introduces effects such as hysteresis, drift and creep which adversely affect the performance of the device. System tools have been applied to study these effects and compensate for them [19]. The PID-design, which is typically employed for control in these devices is inadequate, in many cases, to realize their full potential. Consequently, robust control tools are proposed and implemented which have shown substantial improvement in *simultaneously* achieving fine resolution, high bandwidth and robustness of these devices [16, 17]. The need for high throughputs in many applications has imposed severe demands on these devices. Several system theoretic methods are being applied to address this need, for e.g., increasing the detection bandwidth using observer based control scheme in [20]; and increasing the throughput by implementing an array of cantilevers by using analysis and control tools from the area of distributed control theory [21, 22].

Contribution of the proposed work

Presented research work addresses three fundamental issues of AFM imaging: limitation imposed on imaging bandwidth by physical dynamics of piezo-scanner in contact mode imaging, uncertainty in imaging accuracy due to dynamic characteristic of micro-cantilever in intermittent contact mode and anchoring live cells with rigid cell wall on flat surfaces for quantitative study in dynamic mode AFM imaging.

Solution to fundamental limitation imposed by vertical scanner dynamics: zero error sample profile estimate at any scanning speed*

Researchers have tried to address this issue from first principle: by devising faster scanners. Where they have been successfully pushing the limit further, proposed solutions are always limited by inertia of the piezo scanner due to its finite physical dimension. In this thesis, we derived a causal real-time sample profile estimation scheme that achieves an optimal tip-sample force regulation with an ideal topography image reconstruction at any bandwidth, limited only by accuracy of the dynamic model of the vertical piezo scanner by using systems approach.

It addresses the problem of obtaining accurate sample profiles when scanning at high bandwidth while maintaining a constant cantilever-tip sample force in atomic force microscopes. It is shown that the proposed scheme provides a faithful replica of the sample at ***all relevant scanning speeds*** limited only by the inaccuracy in the model for the atomic force microscope.

In this design scheme, the objective of maintaining a constant tip-sample force while scanning at high bandwidth does not impose limitations on the reconstruction of the sample topography. We have analytically demonstrated that, new scheme can estimate the sample profile with zero error at any scanning speed, as long as the AFM model is accurate.

This provides a paradigm shift where we focused on circumventing fundamental physical limitation by utilizing model of the systems dynamics. This is a new approach to achieve faster imaging over existing designs where the sample profile reconstruction is typically bandwidth limited.

The experimental results corroborate the theoretical development. Therefore, this scheme removed the fundamental limitation of scanning bandwidth imposed by physical dynamics of vertical piezo scanner in contact mode AFM. New scheme achieved **two orders** improvement

*limited by modeling accuracy

in imaging bandwidth without any hardware modification of the existing scanner. Scan rate may be extended to any bandwidth as long as dynamic model of vertical scanner may be accurately determined.

Solution to fundamental limitation imposed by cantilever dynamics: First quantitative measure to detect sensor loss in AFM

Cantilever dynamics is one of the limiting factors in imaging reliability and bandwidth in intermittent contact mode (also known as dynamic mode and Tapping mode AFM (TM-AFM) imaging. Conventional dynamic mode AFM imaging depends on steady state amplitude and phase of the cantilever for reconstructing the surface profile. Dependence on steady state parameters makes dynamic mode AFM imaging vulnerable to inaccuracies during transient state of the cantilever.

A real-time scheme has been developed to identify the areas of the dynamic mode image, where cantilever can not act effectively as a sensor. Considering cantilever itself is the only sensor of sample topography in the AFM system, it is fundamentally challenging to use cantilever's own output to detect its ineffectiveness. An observer based scheme has been developed to identify the areas where cantilever is an effective sensor for the sample topography. This solution addresses a fundamental issue of developing quantitative measure of image fidelity.

Quantitative study of yeast morphology

Although it is widely used for imaging live animal cells, there are relatively fewer reports on AFM imaging of yeast cells ([23], [24]). Yeasts have thick and mechanically strong cell walls and therefore difficult to attach to a solid substrate. In this report, a new immobilization tech-

nique for quantitative imaging and topographic characterization of living yeast cells in solid media using Atomic force microscope (AFM) is presented. Unlike previous techniques, proposed technique allows almost complete cell surface to be exposed to environment and studied using AFM. Apart from the new immobilization protocol, in this report, for the first time, high resolution height imaging of live yeast cell surface in intermittent contact mode is presented. High resolution imaging and significant improvement in operational stability facilitated investigation of growth patterns and evolution of surface morphology in quantitative terms. There is a strong motivation of determining evolution of cell surface morphology to study effect of cell aging on cell surface and this report is a significant step toward this challenging objective.

CHAPTER 2. SYSTEMS SOLUTION TO FUNDAMENTAL LIMITATION ON IMAGING BANDWIDTH IN CONTACT MODE PROFILE ESTIMATION

An optimal control problem is proposed for the control of AFMs which includes the design of a sample-profile estimate signal in addition to the set-point regulation and resolution objectives. A new estimate signal for the sample profile is proposed and it is proved that the transfer function between the profile signal and the estimate signal is unity. Experimental results are presented to corroborate these results.

In this chapter, we address the problem of obtaining accurate estimates of the sample-surface profiles, especially for fast imaging applications. It forms an important step toward building a robust high precision microscope with ultrafast imaging capability. Typically, the control signal u which is the input to the vertical positioner is used as an estimate for the profile, which provides good images for slow scans but proves to be unsatisfactory for fast scans of rough surfaces. [15] presents an elegant idea of using a simulation of the positioner dynamics to obtain better estimates for the sample profile. However this leads to added complexity in the design and is more susceptible to model uncertainties. In [16], the idea of using better sample-profile estimate signals instead of u is presented. These signals are considerably better for fast scans but are still bandwidth limited. The main contribution of this work is that we

Modified from a paper published in *International Journal of Robust and Nonlinear Control*[25]

propose a new estimate signal and prove that it asymptotically tracks the profile perfectly for *all* frequencies - i.e., the transfer function between the estimate signal and the sample profile signal is equal to one!

The proposed signal is obtained by exploiting the ‘quasi-observer’ form of the central \mathcal{H}_∞ -controller and the structure of the model for the device. It comes at no extra computational cost over the control design - The \mathcal{H}_∞ controller is designed to obtain set point regulation and high resolution and the proposed profile estimate signal is derived in terms of this controller. This scheme is demonstrated by simulation and experimental results.

An optimal control problem is proposed which includes the objectives of high resolution, set point regulation and low profile estimation error. We show that the proposed signal is a solution to this problem and study its robustness to modeling uncertainties.

2.1 Setup and Problem Formulation

A schematic of an AFM and its working principle is illustrated in Figure 1.1. Typically AFM is used in either of the two modes of operations - the *dynamic* mode in which the cantilever is made to oscillate and the changes to the periodic orbit due to tip-sample interactions give a measure of the sample profile. In *contact* mode, the cantilever tip rides on the top of the sample and the cantilever deflections due to tip-sample interactions give a measure of the profile. When these deflections are directly used for imaging (the controller in Figure 1.1 is disabled) as in *constant height operation*, the contact forces can vary which typically result in unreliable and distorted images and sometimes tip-sample damage. Therefore in a typical contact mode, the cantilever deflection is regulated at a set-point (i.e. the tip-sample force is kept constant) while scanning the sample surface. This is achieved by moving the vertical

positioner (Z -piezo) to which the cantilever is attached up or down to compensate for the undulations in the sample surface by using a feedback controller. The input to the vertical positioner, i.e. the compensating control signal, is traditionally used as a measure of the sample profile.

However, this method of imaging is valid only for low bandwidth imaging applications. Figure 2.1 shows a system theoretic model of an AFM. Here G_z represents the vertical positioner, G_c represents the microcantilever, S_D represents the deflection transducer and K is the control transfer function. The cantilever tip encounters the surface topography as a time signal $d(t) = h(x(t), y(t))$ where $h(\cdot, \cdot)$ represents the sample profile and $(x(t), y(t))$ denotes the lateral coordinates of the tip sample contact point set by the x - y scanner.

2.2 Modeling tip-sample force as disturbance

This sample profile signal d is viewed as a “disturbance” signal which tries to deviate the cantilever deflection signal from its set point deflection (see Figure 2.1-(A)). We simplify this diagram by combining the transfer functions G_z , G_c and S_D^{-1} as in Figure 2(B). If we assume that G_c is equal to a constant S_C (which is a good approximation since microcantilevers have much larger bandwidths than the vertical scanners), then \tilde{d} represents a scaled sample profile.

The inadequacy of the control signal as an imaging signal at high frequencies is explained by looking at the requirements on control design - it is required that there is good set point regulation to avoid tip-sample damage and retain validity of the model. A good set point regulation over a pre-specified bandwidth is achieved by designing K to have high gain over the bandwidth. This is easily seen from the transfer function from set point r to the regulation error e given by the sensitivity function $S = \frac{1}{1+G(j\omega)K(j\omega)}$ which is small when $|K(j\omega)|$ is large.

Moreover the transfer function from the sample profile \tilde{d} to the control signal u is $\frac{K(j\omega)}{1+K(j\omega)G(j\omega)}$ which is $\approx \frac{1}{G(j\omega)}$ for large K . Typically the positioner transfer function $G(j\omega)$ is approximately a constant at low frequencies and thus the control signal u is a good estimate of the sample profile. However at high frequencies $G(j\omega)$ is not constant and the dynamics of the positioner has to be dealt with. The control signal is clearly an inaccurate estimate of the sample profile at these frequencies. Also note that the temporal frequency content of the \tilde{d} depends on the spatial frequency content of the sample, i.e. how *rough* the sample is, and the scanning rate of the lateral positioners, i.e how *fast* the sample is scanned. In the view of new control designs [18, 19, 16, 17] for faster lateral positioning it is imperative to obtain better estimates of \tilde{d} especially with high frequency content.

2.3 Multi-objective controller design

The control design to use control signal for imaging is seen in conjunction with other important objectives imposed on it. The principal objectives on control design include achieving set-point regulation over high bandwidths, obtaining images with high resolution and keeping control signal within saturation limits of the piezoelectric scanner. High bandwidths are required to maintain a small deflection signal which avoid tip-sample damages in fast scanning of *rough* surfaces (having high spatial frequency content) and to keep the validity of the *linear* model while at the same time stringent resolution requirements impose limitations on bandwidths since a wider bandwidth integrates more sensor noise into the system. It needs to be emphasized that the ultimate goal of microscopy is imaging; the resolution and regulation objectives are futile if the imaging objective is not achieved. In this context, we lay down an optimal control problem which captures all these objectives (See Figure 2.2). In this formula-

tion, the set point regulation, the high resolution and bounded control objectives are captured by the regulated outputs $z_1 = W_S e$, $z_2 = W_T v$, $z_3 = W_u u$ and $z_4 = W_d e_d$ where W_S , W_T and W_u are appropriately chosen weighting functions [26]. The main contribution of this paper is addressing the objective of finding a sample profile estimate. This is captured by requiring the estimate error $W_d(\hat{d} - \tilde{d})$ to be small. Thus the transfer function P from $[r - n \ \tilde{d}]^T$ to z is described by

$$\begin{bmatrix} z_1 \\ z_2 \\ z_3 \\ z_4 \end{bmatrix} = \begin{bmatrix} W_S S & -W_S S \\ W_T T & -W_T T \\ W_u K_1 S & -W_u K_1 S \\ W_d K_2 S & -W_d(1 + K_2 S) \end{bmatrix} \begin{bmatrix} r - n \\ \tilde{d} \end{bmatrix} \quad (2.1)$$

where $S = \frac{1}{1+GK_1}$ is the sensitivity and $T = 1 - S$ is the complementary sensitivity function.

These multiple objectives on control design are met by solving the following \mathcal{H}_∞ problem:

$$\arg \min_{K=[K_1 \ K_2]^T} \|P\|_\infty. \quad (2.2)$$

In practice, for the sake of computational simplicity, we relax this problem in which we seek a sub optimal controller that satisfies $\|P\|_\infty < \gamma$ for some $\gamma > \min_K \|P\|_\infty$. Note that the optimal control problem seeks a *two by one* transfer function $K = [K_1 \ K_2]^T$ where K_1 decides set point regulation, resolution and control within saturation objectives while K_2 decides the extent of sample estimation error.

2.4 Generalized version to estimate disturbance signal

The problem set up presented here can be further generalized by assuming K to have a feedforward term. In the formulation presented, K has access to the deflection signal $e = r - (y + n)$, while the formulation which includes feedforward term can separately provide

the set point r and measured output $y_m := y + n$. However in the context of the objectives discussed in this paper, the lack of feedforward controller does not create any lack of generality. This is because this paper does not have *tracking* as an objective but instead has only *set point regulation* as an objective. However two degrees of freedom controllers do become important when tracking becomes necessary - for instance, in [27] where feedforward law operates to compensate for the sample topography by predicting the topography in advance by taking advantage of the fact that two adjacent scan lines are usually quite similar.

Remark Note that the model in Figure 2.2, the noise n and the disturbance \tilde{d} are indistinguishable to the controller K_2 and therefore the problem of separating the noise and the profile is not addressed by the design of K_2 . However W_d can be appropriately designed to filter out the noise.

2.5 A New Sample-Profile Signal

In this section we prescribe a profile estimate signal \hat{d} . The main features of this signal are (a) It gives a perfect tracking of the sample profile in the sense that the transfer function from profile \tilde{d} to \hat{d} is equal to one! (b) It does not create any additional complexity to the control design - in the sense that \hat{d} is prescribed in terms of signals that appear when solving the \mathcal{H}_∞ problem only with the first three objectives (set point regulation, high resolution and bounded control); i.e. this prescription of \hat{d} renders the fourth objective of small estimation error redundant. (c) Since new estimator block does not enter the closed loop, closed loop performances remain unaffected.

The signal \hat{d} is obtained by analyzing the \mathcal{H}_∞ feedback law designed only for the first three

objectives, i.e. $\left\| \begin{array}{c} W_S S \\ W_T T \\ W_u K_1 S \end{array} \right\|$ and exploiting its quasi-observer structure. It also exploits that the disturbance signal enters the plant G dynamics only in its output and not in its state evolution equation. If the state-space representations of G and the weighting functions are given by

$$G = \left[\begin{array}{c|c} A_g & B_g \\ \hline C_g & D_g \end{array} \right], \quad W_S = \left[\begin{array}{c|c} A_s & B_s \\ \hline C_s & D_s \end{array} \right], \quad W_T = \left[\begin{array}{c|c} A_t & B_t \\ \hline C_t & D_t \end{array} \right] \text{ and } W_u = \left[\begin{array}{c|c} A_u & B_u \\ \hline C_u & D_u \end{array} \right], \quad (2.3)$$

then the corresponding generalized plant P is described by:

$$\begin{aligned} \begin{bmatrix} \dot{x}_g \\ x_s \\ x_t \\ x_u \end{bmatrix} &= \underbrace{\begin{bmatrix} A_g & & & \\ -B_s C_g & A_s & & \\ B_t C_g & 0 & A_t & \\ & & & A_u \end{bmatrix}}_{\triangleq A} \underbrace{\begin{bmatrix} x_g \\ x_s \\ x_t \\ x_u \end{bmatrix}}_{\triangleq x} + \underbrace{\begin{bmatrix} 0 \\ B_s \\ 0 \\ 0 \end{bmatrix}}_{\triangleq B_1} w + \underbrace{\begin{bmatrix} B_g \\ -B_s D_g \\ B_t D_g \\ B_u \end{bmatrix}}_{\triangleq B_2} u \\ \begin{bmatrix} z_1 \\ z_2 \\ z_3 \end{bmatrix} &= \underbrace{\begin{bmatrix} -D_s C_g & C_s & & \\ D_T C_g & 0 & C_t & \\ & & & C_u \end{bmatrix}}_{\triangleq C_1} \underbrace{\begin{bmatrix} x_g \\ x_s \\ x_t \\ x_u \end{bmatrix}}_{\triangleq x} + \underbrace{\begin{bmatrix} D_s \\ 0 \\ 0 \end{bmatrix}}_{\triangleq D_{11}} w + \underbrace{\begin{bmatrix} -D_s D_g \\ D_t D_g \\ D_u \end{bmatrix}}_{\triangleq D_{12}} u \\ e &= \underbrace{\begin{bmatrix} -C_g & 0 & 0 & 0 \end{bmatrix}}_{\triangleq C_2} \underbrace{\begin{bmatrix} x_g \\ x_s \\ x_t \\ x_u \end{bmatrix}}_{\triangleq x} + \underbrace{[I]}_{\triangleq D_{21}} w - \underbrace{D_g}_{\triangleq D_{22}} u, \end{aligned} \quad (2.4)$$

where $w = r - n - \tilde{d}$ (Here we consider set point r to be 0 without any loss of generality and do not consider the effect of noise n . Its effect is considered in the next section).

2.6 Controller design from H-infinity synthesis procedure

The \mathcal{H}_∞ synthesis procedure ([26],[28],[29]) yields a controller K_1 which can be written as an observer-based state feedback

$$\dot{\hat{x}} = (A + B_1 F_{12\infty} + Z_\infty L_{2\infty} F_{12\infty})\hat{x} + B_2 u + Z_\infty L_{2\infty} \underbrace{(C_2 \hat{x} + D_{22} u - e)}_{\triangleq \hat{e}} \quad (2.5)$$

$$u = F_{2\infty} \hat{x}. \quad (2.6)$$

Here the matrices $Z_\infty, F_{12\infty}, F_{2\infty}$ and $L_{2\infty}$ are described in [28] p.p. 451-52. We define the estimate \hat{d} of the deflection signal \tilde{d} by $\hat{d} \triangleq \hat{e} - e$, where $\hat{e} = C_2 \hat{x} + D_{22} u$ is the estimate of the error, e . Therefore, if we define the state estimation error, $\tilde{x} \triangleq x - \hat{x}$ and the profile estimation error by $e_d \triangleq \hat{d} - \tilde{d}$, then

$$e_d = \hat{d} - \tilde{d} = (C_2 \hat{x} + D_{22} u) - (C_2 x + D_{22} u - \tilde{d}) - \tilde{d} = -C_2 \tilde{x}$$

From Equations (2.4) and (2.5), we have

$$\begin{aligned} \dot{\tilde{x}} &= A\tilde{x} + B_1(w - F_{12\infty}\hat{x}) + Z_\infty L_{2\infty} F_{12\infty} \tilde{x} + Z_\infty L_{2\infty} (d - F_{12\infty}\hat{x}) \\ \Rightarrow E_d(s) &= -C_2 \tilde{x}(s) \\ &= -\underbrace{(C_2(sI - A - Z_\infty L_{2\infty} C_2)^{-1} B_1(w - F_{12\infty}\hat{x}))}_{\triangleq E_1(s)} + \underbrace{C_2(sI - A - Z_\infty L_{2\infty} C_2)^{-1} Z_\infty L_{2\infty} (d - F_{12\infty}\hat{x})}_{\triangleq E_2(s)}. \end{aligned}$$

2.7 Zero error in disturbance (or profile) estimation for all bandwidth

Since, $e_d = -C_2 \tilde{x}$, and \tilde{x} is the state of a stable system, we expect the e_d to be small. But we prove a stronger result - that $E_1(s) = 0$ and $E_2(s) = 0$ by exploiting the structure of the generalized plant!

Lemma 2.7.1 *When all matrices and transfer functions are defined as in [28] p.p. 451-52, G is a stable strictly proper transfer function and all W_s, W_T and W_u are stable, $D'_{o1} \tilde{R}^{-1} D_{o1} = 1$*

Proof

Note that,

$$D_{\circ 1} = [D_s \ 0 \ 0 \ 1]$$

and

$$\tilde{R} = D_{\circ 1} D'_{\circ 1} - \begin{bmatrix} \gamma^2 I & 0 \\ 0 & 0 \end{bmatrix}$$

Since γ and D_s are scalar, using standard inversion technique,

$$\tilde{R}^{-1} = \begin{bmatrix} -1/\gamma^2 & 0 & 0 & D_s/\gamma^2 \\ 0 & -1/\gamma^2 & 0 & 0 \\ 0 & 0 & -1/\gamma^2 & 0 \\ D_s/\gamma^2 & 0 & 0 & (-D_s^2 + \gamma^2)/\gamma^2 \end{bmatrix}$$

therefore,

$$\begin{aligned}
D'_{o1} \tilde{R}^{-1} D_{o1} &= D'_{o1} \begin{bmatrix} -1/\gamma^2 & 0 & 0 & D_s/\gamma^2 \\ 0 & -1/\gamma^2 & 0 & 0 \\ 0 & 0 & -1/\gamma^2 & 0 \\ D_s/\gamma^2 & 0 & 0 & (-D_s^2 + \gamma^2)/\gamma^2 \end{bmatrix} D_{o1} \\
&= (-D_s/\gamma^2 + D_s/\gamma^2) D_s + D_s^2/\gamma^2 + (-D_s^2 + \gamma^2)/\gamma^2 \\
&= 1
\end{aligned}$$

Lemma 2.7.2 *When all matrices and transfer functions are defined as in [28] p.p. 451-52, G is a stable strictly proper transfer function and all W_s, W_T and W_u are stable, $Y_\infty = 0$*

Proof As per [28], let's define

$$J_\infty = \begin{bmatrix} A^* & 0 \\ -B_1 B_1^* & -A \end{bmatrix} - \begin{bmatrix} \times \\ -B_1 D_{o1}^* \end{bmatrix} \tilde{R}^{-1} [D_{o1} B_1^* \quad \times]$$

Since according to Lemma 2.7.1, $D'_{o1} \tilde{R}^{-1} D_{o1} = 1$

$$\begin{bmatrix} \times \\ -B_1 D_{o1}^* \end{bmatrix} \tilde{R}^{-1} [D_{o1} B_1^* \quad \times] = \begin{bmatrix} \times & \times \\ -B_1 B_1^* & \times \end{bmatrix} -$$

Hence,

$$\begin{aligned}
J_\infty &= \begin{bmatrix} A^* - \times & \times \\ -B_1 B_1^* + B_1 B_1^* & -A - \times \end{bmatrix} \\
&= \begin{bmatrix} A^* - \times & \times \\ 0 & -A - \times \end{bmatrix}
\end{aligned}$$

Comparing RHS with standard form of ARE,

$$\underbrace{\begin{bmatrix} \bar{A} & R \\ -Q & -\bar{A}^* \end{bmatrix}}_{\text{Hamiltonian of ARE}}$$

We conclude that $Q = 0$.

Therefore, one solution of the second ARE is zero, i.e.

$$\begin{aligned}
Y_\infty &:= Ric(J_\infty) \\
&= 0
\end{aligned}$$

Lemma 2.7.3 *When all matrices and transfer functions are defined as in [28] p.p. 451-52,*

G is a stable strictly proper transfer function and all W_s, W_T and W_u are stable, $Z_\infty = 1$ and

$L_{2\infty}$ is of the form: $B_1 \times$

Proof From Lemma 2.7.2:

$$Y_\infty = 0$$

Therefore,

$$\begin{aligned} Z_\infty &:= (I - \gamma^{-2} Y_\infty \times)^{-1} \\ &= I \end{aligned}$$

and

$$\begin{aligned} L_{2\infty} &:= -[B_1 D_{o1}^* + Y_\infty C^*] \tilde{R}^{-1} \\ &= -[B_1 D_{o1}^*] \tilde{R}^{-1} \\ &= B_1 \times \end{aligned}$$

Theorem 2.7.4 *Let G be a stable strictly proper transfer function and W_s, W_T and W_u be stable transfer functions. Then, $E_d(s) \equiv 0$*

Proof

$$\begin{aligned} \dot{\tilde{x}} &\triangleq x - \hat{x} \\ &= A\tilde{x} + B_1(w - F_{12\infty}\hat{x}) \\ &\dots + Z_\infty L_{2\infty} F_{12\infty} \tilde{x} \\ &\dots + Z_\infty L_{2\infty} (d - F_{12\infty}\hat{x}) \end{aligned}$$

$$\Rightarrow E_d(s) = -C_2 \tilde{x}(s)$$

$$= -(C_2(sI - A - Z_\infty L_{2\infty} C_2)^{-1} B_1 (w - F_{12\infty} \hat{x}))$$

$$+ C_2(sI - A - Z_\infty L_{2\infty} C_2)^{-1} \overbrace{Z_\infty L_{2\infty}}^{=B_1 \times [\cdot \cdot] \text{ (by Lemma 2.7.2)}} (d - F_{12\infty} \hat{x}))$$

$$\begin{aligned} &= -\underbrace{(C_2(sI - A - Z_\infty L_{2\infty} C_2)^{-1} B_1 (w - F_{12\infty} \hat{x}))}_{\triangleq E_1(s)} \\ &\quad + \underbrace{C_2(sI - A - Z_\infty L_{2\infty} C_2)^{-1} B_1 \times [\cdot \cdot] (d - F_{12\infty} \hat{x}))}_{\triangleq E_2(s)} \end{aligned}$$

It may be shown that when u and v are column vectors: $(I - uv')^{-1} \equiv I + \frac{uv'}{1-v'u}$. This matrix identity may be utilized to simplify E_1 and E_2 .

$$\begin{aligned} & C_2(sI - A - Z_\infty L_{2\infty} C_2)^{-1} B_1 \\ &= C_2(sI - A)^{-1} \left(I - \underbrace{Z_\infty L_{2\infty}}_u \underbrace{C_2(sI - A)^{-1}}_{v'} \right)^{-1} B_1 \\ &= C_2(sI - A)^{-1} \left(I + \frac{Z_\infty L_{2\infty} C_2(sI - A)^{-1}}{1 - C_2(sI - A)^{-1} Z_\infty L_{2\infty}} \right) B_1 \\ &= \frac{C_2(sI - A)^{-1} B_1}{1 - C_2(sI - A)^{-1} Z_\infty L_{2\infty}} + \left(\frac{C_2(sI - A)^{-1} Z_\infty L_{2\infty} C_2(sI - A)^{-1}}{1 - C_2(sI - A)^{-1} Z_\infty L_{2\infty}} \right) B_1 \\ &= \frac{C_2(sI - A)^{-1} B_1}{1 - C_2(sI - A)^{-1} Z_\infty L_{2\infty}} + \left(\frac{C_2(sI - A)^{-1} B_1 \times [\cdot \cdot] C_2(sI - A)^{-1}}{1 - C_2(sI - A)^{-1} Z_\infty L_{2\infty}} \right) B_1. \end{aligned}$$

Therefore, numerators of E_1 and E_2 are of the form:

$$\underbrace{C_2(sI - A)^{-1}B_1}_{\text{to show: equal to zero}} \times [\cdot \cdot]$$

Since A is a lower triangular matrix, so is $(sI - A)$. Therefore $(sI - A)^{-1}$ is a lower triangular matrix. Hence, $(sI - A)^{-1}$ may be written in the form of:

$$\begin{bmatrix} \times & 0 \\ \times & \times \end{bmatrix}$$

Hence,

$$\begin{aligned} E_d &= \frac{C_2(sI - A)^{-1}B_1}{(\dots)} \times [\cdot \cdot] \\ &= \frac{1}{(\dots)} \begin{bmatrix} -C_g & 0 \end{bmatrix} \begin{bmatrix} (sI - A_g)^{-1} & 0 \\ \times & \times \end{bmatrix} \begin{bmatrix} 0 \\ \times \end{bmatrix} [\cdot \cdot] \\ &= \frac{1}{(\dots)} \begin{bmatrix} -C_g & 0 \end{bmatrix} \begin{bmatrix} 0 \\ \times \end{bmatrix} [\cdot \cdot] \\ &= 0. \end{aligned}$$

This means that $E_d(s) = 0$ which implies that \hat{d} tracks \tilde{d} of arbitrarily large frequencies. In typical AFM designs the estimates of the sample profile, \tilde{d} is obtained by processing the control signal u (as in ‘constant force mode’) or the deflection signal y_m (as in the ‘constant height mode’). The profile estimate \hat{d} , on the other hand, derives information from *both* u and y_m . Note that \hat{d} is prescribed only in terms of signals arising out of design of K_1 . Consequently K_2 is obtained in terms of matrices representing K_1 by using (2.5),

$$K_1 = F_{2\infty}(sI - A - B_1F_{12\infty} - B_2F_{2\infty} - Z_\infty L_{2\infty}(F_{12\infty} + C_2 + D_{22}F_{2\infty}))^{-1}Z_\infty L_{2\infty}$$

$$K_2 = -(1 + (C_2 + D_{22}F_{2\infty})(sI - A - B_1F_{12\infty} - B_2F_{2\infty} - Z_\infty L_{2\infty}(F_{12\infty} + C_2 + D_{22}F_{2\infty}))^{-1}Z_\infty L_{2\infty})$$

and since $E_d(s) = -(K_2S + 1)\tilde{d} = 0$, therefore $K_2S = -1$. In this context the profile estimate using \mathcal{H}_∞ design does provide many advantages: (a) it is easy to design as there is plenty of

commercial software that solves these optimal control problems and (b) as the signal estimate transfer function K_2 in Figure 2.2 comes as a consequence of design of K_1 and does not require any explicit computation- i.e. the profile estimate \hat{d} is prescribed in terms of the internal signals (\hat{e} and e) in the loop itself and thus does not add to the computational burden in the design procedure. Another important aspect of this design is that the class of controllers that attain the first three objectives are given by lower Linear Fractional Transformation (LFT) $\mathcal{F}_l(K_1, Q)$ where $Q(s)$ is any stable proper transfer function such that $\|Q\|_\infty \leq \gamma$ where γ is performance bound as described at the end of the section 2.1. Since K_2 is completely specified by K_1 , this also gives a parametrization of all the controllers that satisfy all the objectives in (2.2).

2.8 Robustness of this signal to plant uncertainties

An important aspect of control design in AFM is robustness. It is especially important since the unmodeled nonlinear effects of piezoactuation such as drift and hysteresis are significant; and these devices are used in diverse operating conditions which necessitate robustness to these uncertainties. We consider a modified block diagram shown in Figure 2.3 to study robustness of the prescribed control design with respect to modelling uncertainties. In this model G is modified to include input and output multiplicative uncertainties. The matrix transfer function from $[r - n \tilde{d}]$ to the vector of regulated variables $z \triangleq [z_1 \ z_2 \ z_3 \ z_4]^T$ (is the same as given in (2.1)) describes the nominal performance.

2.9 Effect of measurement noise in profile estimation

The control design prescribed in previous section ensures that the transfer functions $\|W_S S\| < 1$, $\|W_T T\| < 1$ and $\|W_u K_1 S\| < 1$. Moreover, the proposed choice of K_2 is such that $K_2 S = -1$.

Thus by choosing the weighting function W_d such that it is small at those frequencies where noise is significant we guarantee all the nominal performance objectives. The noise n and the disturbance \tilde{d} are indistinguishable to the controller and therefore an appropriate filter W_d is required to separate out the two. The transfer function from perturbation inputs $\theta \triangleq [\theta_1 \ \theta_2]$ to the regulated variables z describes the robust performance:

$$\begin{bmatrix} z_1 \\ z_2 \\ z_3 \\ z_4 \end{bmatrix} = \begin{bmatrix} -W_S G S & -W_S S \\ W_T G S & -W_T S \\ -W_u T & W_u K_1 S \\ -W_d G K_2 S & -W_d K_2 S \end{bmatrix} \begin{bmatrix} \theta_1 \\ \theta_2 \end{bmatrix}.$$

The control design for nominal performances for set point regulation, boundedness of control, and profile estimation error also guarantees robustness with respect to output uncertainty (with θ_2). The effect of θ_2 on z_2 given by $W_T S$ is not small but this is expected as this model fails to distinguish the output uncertainty (θ_2 which is akin to sensor noise) and the disturbance signal \tilde{d} . The robustness to input uncertainty (to θ_1) suggests a careful design of K to account for the trade off between nominal and robust performances. Thus designing W_S , W_T and W_d so that they shape GS , GK_1S and GK_2S instead of S , K_1S and K_2S respectively ensures robust performance of bandwidth, boundedness of control and profile estimation with respect to the input uncertainty. This is evident from the fact that in SISO system we can easily lump together the input and output uncertainties by transferring the input uncertainties to the output side via the plant transfer function G [26]. The transfer function from θ_2 to $[z_1 \ z_2]^T$ further shows that there is a trade off between the robustness in set point regulation and high resolution with respect to input uncertainty. This trade off is captured by the fact that robust performance of both requires $W_S G S$ and $W_T G S$ to be small simultaneously. The transfer function from $[\theta_1 \ \theta_2]^T$ to e_d evaluates robust performance of the proposed design. Note that since $1 + K_2 S = 0$, W_d needs to be chosen so as to make W_d small at the frequencies where

n and θ_2 are significant and to make $W_d G$ small at those frequencies where θ_1 is significant. This can easily be incorporated without making any compromise on the transfer function from sample profile \tilde{d} to the estimation error z_4 which remains equal to zero!

It should be emphasized that input uncertainty is not as significant as the output uncertainty as illustrated in Section 2.11.

2.10 Observer Based Designs

The \mathcal{H}_∞ design presented here finds a solution to an optimal problem which makes it unnecessary to study other designs. However, the model in which the sample profile is viewed as a disturbance signal as in Figure 2.1 immediately suggests an observer based design for disturbance estimation. Also the similarity in the structures of the controllers in \mathcal{H}_∞ and the observer designs gives a good motivation to study the latter. The various trade offs between the regulation, robustness and profile estimation have close analogues in the \mathcal{H}_∞ design. This provides a good motivation to study observer based designs. In this section we propose profile estimate signals based on observer based designs and analyze them.

A schematic of this design is illustrated in Figure 2.4(A). The basic idea is to exploit the difference between the deflection signal $e = C_2 x + \tilde{d}$ (where $\bar{d} = \tilde{d} + n$, the notation for states and generalized plant is the same as in (2.4)) and its estimate $\hat{e} = C_2 \hat{x}$. Therefore, when the state estimate error $x - \hat{x}$ goes to zero - the corresponding difference in deflection signal $\hat{d} \triangleq \hat{e} - e$ goes to \bar{d} ; or equivalently the profile estimation error $e_d \triangleq \hat{d} - \tilde{d}$ goes to zero. The control design is translated to finding gain matrices F and L such that the profile estimation error e_d is small while maintaining the deflection signal at the set point and at the same time ensuring robustness of these objectives to modeling uncertainties in G .

Glover-McFarlane Design

This design yields a controller that has an observer structure and thus lends itself to the design of the estimation signal \hat{d} . This methodology is specifically used for providing robustness to systems which already have controllers in place which achieve certain performance objectives (say set point regulation). A remarkable feature of this design is that it achieves robustness with marginal reduction in performance [30, 31]. In fact, it is able to quantify the reduction by determining explicit bounds on how much it changes the loop gains at low and high frequencies. This design process consists of two steps - (a) Design for performance: In this step, a shaping transfer function K_s is designed to meet the performance requirements. At this stage the requirements for robustness and even stability are not considered. In the context of this paper K_s can be thought of as an already existing controller that achieves set point regulation. (b) Design of a robustifying controller: In this step, a robustifying controller K_r is obtained which gives good robustness properties to the closed loop system obtained from the shaped plant $G_s = K_s G_{xx}$ of the previous step. More specifically let $G_s = \frac{N}{M}$ be the normalized coprime factorization of the nominal shaped plant. The normalized coprime factor uncertainty characterization (see Figure 2.5) is given by,

$$\left\{ \frac{N + \Delta_N}{M + \Delta_M} : \left\| \begin{bmatrix} \Delta_N & \Delta_M \end{bmatrix} \right\| \leq \epsilon \right\},$$

The robustifying controller stabilizes all the plants belonging to the above set for a specified ϵ . For a shaping controller K_s , the maximum possible ϵ , ϵ_{max} can be calculated a priori as shown below. The robustness margin $\frac{1}{\gamma}$ is chosen to be slightly less than ϵ_{max} .

In this setting with the shaping controller given by $\left(\begin{array}{c|c} A_s & B_s \\ \hline C_s & D_s \end{array} \right)$, the AFM system de-

scribed in Figure 2.5 is given by

$$\begin{aligned} \begin{bmatrix} \dot{x}_g \\ \dot{x}_s \end{bmatrix} &= \underbrace{\begin{bmatrix} A_g & B_g C_s \\ 0 & A_s \end{bmatrix}}_A \begin{bmatrix} x_g \\ x_s \end{bmatrix} + \underbrace{\begin{bmatrix} B_g D_s \\ B_s \end{bmatrix}}_B u \\ e &= \underbrace{\begin{bmatrix} -C_g & 0 \end{bmatrix}}_C \begin{bmatrix} x_g \\ x_s \end{bmatrix} - \bar{d} \end{aligned} \quad (2.7)$$

The robustifying controller is an observer:

$$\hat{x} = A\hat{x} + Bu + L(C\hat{x} - e)$$

$$u = F\hat{x}$$

where the observer gain $L = -ZC^T$ and the regulator $F = -\gamma^2 B^T[(\gamma^2 - 1)I - XZ]^{-1}X$ and $\gamma^2 - 1$ is the spectral radius of the product XZ and the matrices X and Z are given by the AREs:

$$\begin{aligned} AZ + ZA^T - ZC^T CZ + BB^T &= 0 \\ A^T X + XA^T - XBB^T X + C^T C &= 0. \end{aligned}$$

The profile estimate is given by $\hat{d} = \hat{e} - e$ and therefore transfer function from \tilde{d} to estimation error $e_d = \hat{d} - d$ is given by $T_{e_d \tilde{d}} = C(sI - A - ZC^T)^{-1}ZC^T$. In this design, note that this transfer function is not zero and it depends significantly on the shaping transfer function K_s . Here a reduced performance in profile estimation is traded for further robustness towards plant uncertainty. Of particular interest is pole-zero uncertainty (well captured by coprime uncertainty characterization) which is of significance in piezo actuated flexure stages typically employed in AFMs. Even with this reduced profile estimation capability experimental results reported in [16] show estimate signals based on the Glover McFarlane design show a marked improvement in the profile estimate over using the control signal.

The Glover McFarlane design has the advantage of modifying *existing* designs besides providing for robustness. They are especially useful for plants where there is severe pole uncertainty and the resonances are lightly damped [32]. This difference is critical in view \mathcal{H}_∞ designs which typically tend to invert the dynamics of the plant model. However, in all these observer based methodologies, the control design to *simultaneously* achieve *multi-objectives* proves to be difficult. Consequently the disadvantages in these designs outweigh the advantages they have over the \mathcal{H}_∞ design. In the next section we present the experimental set up, the implementation of the controller resulting from the H_∞ design and show experimental imaging results with the proposed signal.

2.11 Experimental Setup and Results

The experiments were performed using MFP-3D developed by *Asylum Research, Inc.* A schematic of this device is given in Figure 2.6(A). Its main components are a micro-cantilever, XY and Z positioning stages. A detailed description of the XY positioning stage can be found in [33]. The cantilever used is approximately 120 μm long, 5 μm width and its tip is approximately 10 – 20 nm in diameter. The resonant frequency of the cantilever is 13.25 kHz . Imaging procedure is the same as described in section 2.1. The device is modified to implement the proposed control (\mathcal{H}_∞) design through a software interface which was used to set up control parameters and to acquire and analyze the data (see Figure 2.6 (B)). The cantilever deflection is sampled at 5MHz and recorded. A custom DSP code for proposed controller is implemented on ADSP-21160 DSP chip. This DSP code takes the deflection data as input and generates scaled down actuation signal (z-piezo actuation requires high voltage, beyond range of DACs of the DSP chip.). After amplification, this actuation signal is applied across the Z-piezo.

The voltage range of Z-piezo is -10V to 150V and travel range is 100 μm . The uncertainty in the input signal is mainly contributed by DAC and uncertainty in piezo dynamics. Given 16 bit precision (Range of DAC (20 V) $\times \frac{1}{2^{16}} \times$ sensitivity (100 nm/V) = .03nm) in DAC and small range movement reliability of piezo (sub-angstrom), output uncertainty outweighs input uncertainty. The output signal is mainly corrupted by photo-diode noise, surface vibration and acoustic noise which add up to 0.5 – 0.8 nm.

2.11.1 System identification

The control interface was used to implement the scheme described in Figure 2.2. The transfer function from u the input to the Z-piezo to the measured output y_m was obtained using frequency based identification techniques. Here, we chose a specific point in the operating range of the device (where its behavior is approximately linear) and obtain a model of the device at this point by studying its frequency response over a prespecified bandwidth. For this purpose, we used a HP signal analyzer, which gave a series of sinusoidal inputs, $u = A \sin(\omega t)$ (V), with frequencies spanning over a bandwidth of 2 kHz. The amplitude of the signals, A were chosen small enough (≤ 500 mV) to be in the linear regime of the device. The frequency response of the device at this operating point is shown in the bode plot (dashed lines) in Figure 2.7.

Accordingly, an eleventh order stable transfer function:

$$G = \frac{-8.208 \times 10^3 (s^2 + 530.9s + 3.132 \times 10^7)(s^2 + 472s + 1.558 \times 10^8)}{(s + 2.513 \times 10^4)(s^2 + 768s + 3.146 \times 10^7)(s^2 + 615.8s + 1.422 \times 10^8)} \\ \times \frac{(s^2 + 868.3s + 2.734 \times 10^8)}{(s^2 + 918.9s + 1.777 \times 10^8)} \\ \times \frac{(s^2 + 249.1s + 3.011 \times 10^8)(s^2 - 2.827 \times 10^4s + 5.021 \times 10^8)}{(s^2 + 508.8s + 2.789 \times 10^8)(s^2 + 377.1s + 3.056 \times 10^8)}$$

was fit to this data. Figure 2.7 shows that there is a good match between this frequency response data and the one fitted to the data, $G(s)$.

2.11.2 Control design, implementation and validation

The control transfer function K_1 was obtained using the *hinf* function in MATLAB. In this design, the weighting function W_S is chosen such that it has high gains at low frequencies and low gains at high frequencies (see Figure 2.8(A)). This scaling ensures that the optimal feedback law is such that the sensitivity function is small at low frequencies, thus guaranteeing good set point regulation at the concerned frequencies. More precisely, W_S was chosen to be a first order transfer function, $W_s(s) = \frac{0.3333s+2199}{s+2.199}$. This transfer function is designed so that its inverse (an approximate upper bound on the sensitivity function) has a gain of $-60dB$ at low frequencies ($< 100 Hz$) and a gain of $\approx 9.5dB$ above $1000 Hz$. The weight W_T was chosen to be $W_T(s) = \frac{s+2199}{10^{-5}s+1.1 \times 10^4}$. which has high gains (100dB) at high frequencies (note that noise is in the high frequency region) to ensure high resolution. The transfer function, K_1S was scaled by a constant weighting $W_u = 40dB$, to restrict the magnitude of the input signals such that they are within the saturation limits. This weighting constant gives control signals that are at most six times the reference signals.

The \mathcal{H}_∞ design resulted in 13th order controllers given by K_1 and K_2 . Figure 2.8(B) shows the controller and observer obtained from the solution of stacked H_∞ problem. Note that K_1 and K_2 have a similar dynamics at low frequencies and therefore give similar images at these frequencies. These transfer functions were implemented onto the DSP and the signals \hat{d}, r , and u were recorded and used to evaluate images. The implementation of the loop was validated by comparing the closed loop transfer functions obtained using HP-Signal analyzer with the simulated ones. Figure 2.9 shows experimental and theoretical frequency response of sensitivity and complementary sensitivity functions. As seen in the figures, experimental and theoretical responses match closely except a particular frequency range around 400 Hz.

2.11.3 Results

To study the performance of the new estimate signal, it was compared to and contrasted with the typically used control signal. Figure 2.10(A) shows that the bandwidth of the transfer function T_{ud} has a bandwidth of approximately 800 Hz where as the magnitude of $T_{\hat{d}d}$ (in Figure 2.10(B)) is within 3 dB for the whole range considered. The phase plots show considerable phase drop for the T_{ud} while near zero phase for the $T_{\hat{d}d}$. This explains the difference seen in the trace and the retrace scans when using the u signal for the image. It is important to note that the bandwidth of 800 Hz for the transfer function T_{ud} is by itself a huge improvement over typical commercial AFMs (which have imaging bandwidth in order of few tens of Hz).

It is shown analytically that $T_{\hat{d}d}$ is identically equal to one - however, the experimental transfer function $T_{\hat{d}d}$ slightly deviates from one (see Figure 2.10). The reason, after careful analysis and experiments, was attributed to the fact that there is an uncertain pole-zero pair (near 400 Hz) in the plant G . On repeating the experiments to obtain the frequency response of G showed that the location of the pole-zero pair is not constant. Since the design presented here is model-based, this uncertainty leads to minor mismatch between the simulations and the experiments. There are other regions in the frequency range where there is a mismatch (though within 3 dB) between sample profile and its estimate. This is again attributed to the inherent constraint of model based controller design. Due to limited computation power, it is not possible (and also not advisable) to fit an arbitrary higher order plant to the physical system. However the sensitivity to this mismatch is incorporated in the design procedure by appropriately shaping the K_2S transfer function.

In addition to investigating the above transfer functions, imaging experiments were performed to test the proposed profile estimate signal. A gold calibration grid with squares of

height 180 nm every $10\mu\text{m}$ was used for imaging using the \hat{d} signal. This image was compared with the one obtained from the control signal u . In the first experiment, the grating was scanned at 10 Hz and the corresponding control signal u and the proposed estimate signal \hat{d} were recorded. The control signal was proportional to the profile, in fact $u \approx -0.1d$. Therefore u signal was magnified by ≈ 10 times to get the profile estimate. The resulting data is shown in Figure 2.11(A). Note that the scanned image with the proposed signal is superior to the image with the u signal. This is more evident in the plots showing a particular line scan, where the image with u has an oscillatory behavior in response to the higher frequency content of the square profile. The main feature of the proposed signal is the high bandwidth it achieves. The difference in performance between the \hat{d} and u signals is much greater in faster scans. This is shown in Figure 2.11(B). Here the scan was done at 150 Hz , 500 Hz and 1400 Hz where the reference signal was generated on the computer itself and downloaded onto the DSP card to mimic a sinusoidal sample profile. At low frequencies (below the bandwidth of T_{ud}) the control signal u is a good measure of d . However, there is a significant phase lag between the d and the u signal at 500 Hz . At higher frequency (1400 Hz) control signal gives a poor estimate of d - it is attenuated (by more than 50%) and has considerable phase lag. The experimental results show that the proposed signal \hat{d} tracks near perfectly the reference signal even at these high bandwidths, as well as in lower frequencies. This fact is corroborated from the frequency response of transfer functions shown in Figure 2.10, where T_{ud} rolls off after 800 Hz with significant phase lag but $T_{\hat{d}d}$ remains with $\pm 3\text{ dB}$ with almost zero phase. This imaging at 1.4 kHz demonstrates a substantial improvement over the existing technology where images are usually scanned at few tens of Hz .

This same algorithm was also implemented on another AFM (DI-AFM built by Veeco

Instruments, Santa Barbara) and experimental results again corroborated that $T_{dd} \approx 1$ (results not shown here).

2.12 Conclusions

The imaging problem in an AFM is addressed using modern control theory. An optimal control problem was formulated to address the design of a new profile estimate signal which is valid even for fast scanning for AFM. The objectives of set point regulation, high resolution and boundedness of control signal are also included in the formulation. The solution of this problem yields a new estimate of the sample profile, \hat{d} and it is *proved* that the transfer function from the profile to the estimate is 1. The designed controllers were implemented and a substantial improvement over the traditional designs is shown. Typical designs in commercial AFM use PID controllers which do not give reliable images beyond a few tens of Hz bandwidth while experiments with the proposed signal at $1400\ Hz$ gave faithful images. Experiments showed a significant improvement in bandwidth in sample-profile estimation. The control signal had a bandwidth of around $800\ Hz$ which by itself is an improvement over typical PID designs, while the frequency response from the profile to the estimation error was near zero for the whole range of frequencies ($\leq 3000\ Hz$).

The proposed signal makes use of *both* the control signal u and the deflection signal e smartly to give the sample profile in contrast to using only the control signal u in constant force imaging and using only the deflection signal e in constant height imaging. A similar idea emerges in [34] for *dynamic mode* of operation where the information from the control signal is used together with the rapidly varying cantilever deflections for imaging. This motivates to develop a method similar to the one presented here to the tapping mode case. Here advanced

control tools have been used to tackle an important imaging problem in AFM. There is a lot of scope for control theoretic tools to improve the bandwidth, resolution and reliability of these devices. There is a clear coupling between the lateral and vertical positioning systems and MIMO designs would prove very successful in achieving these improvements simultaneously.

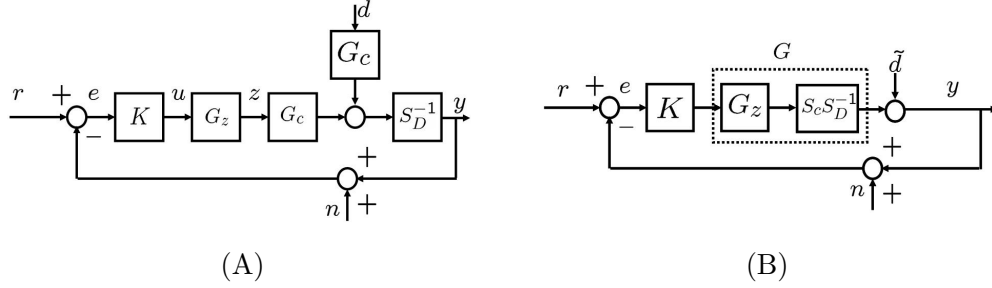


Figure 2.1 (A) shows the block diagram modeling of the AFM where G_c , G_z , K , S_D are the cantilever, piezo-scanner, controller and the deflection transducer transfer functions respectively. The signals r , y , e and n are the setpoint, the cantilever deflection, the deflection error and the transducer noise respectively. The signal d models the sample topography. (B) G represents a combination of the scanner, lever and the transducer dynamics. The cantilever has high resonant frequency and is assumed to be a constant over the frequency region of interest. Hence \tilde{d} is a scaled version of the sample topography

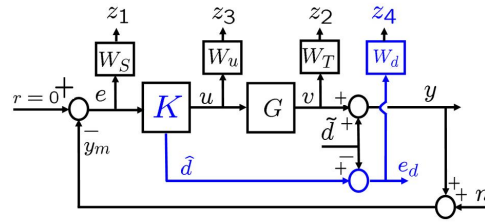


Figure 2.2 Framework for the optimal control problem. The controller $K = [K_1 \ K_2]^T$ has two outputs - the control signal u with the objective of achieving robust set point regulation of the deflection signal y and high resolution through roll off of the transfer function from the setpoint r to the piezo response v ; and the signal \hat{d} with the objective of giving an accurate estimate of the sample profile \tilde{d} . Our design objective is to minimize weighted performance variable z_1 (weighted regulation error), z_2 (weighted noise sensitivity), z_3 (weighted control effort) and z_4 (weighted estimation error)

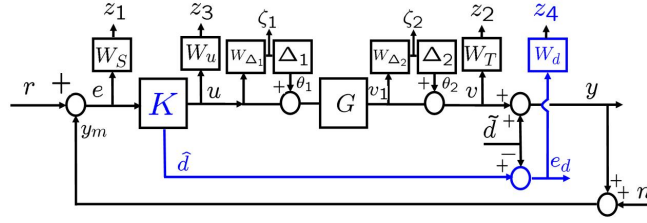


Figure 2.3 The schematic for the Robust \mathcal{H}_∞ framework with output and input multiplicative plant uncertainties.

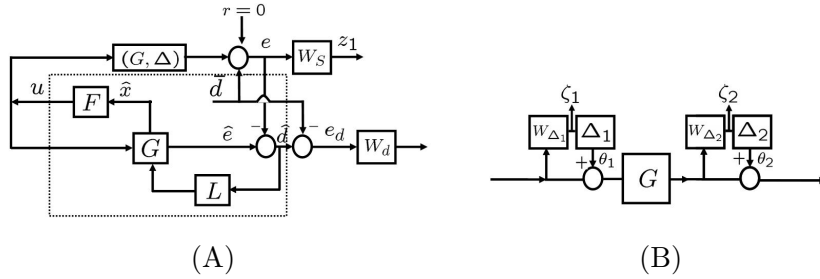


Figure 2.4 (A) A schematic of the observer design - Gain matrices F and L need to be designed to achieve small profile estimation error, set point regulation and robustness with respect to class of plants (G, Δ) . (B) The form of (G, Δ) for input and output multiplicative uncertainties.

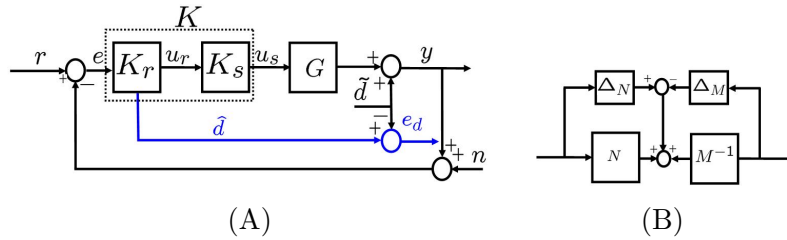


Figure 2.5 (A) Glover McFarlane Design: The controller K has two components - K_s designed exclusively for performance objective such as set point regulation, and K_r designed to achieve robustness of the loop. (B) The form of (G, Δ) . This uncertainty characterization is especially useful to characterize low damped pole uncertainties.

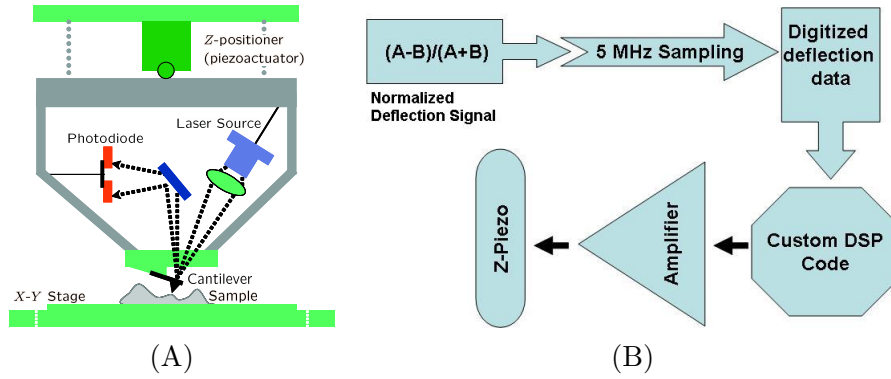


Figure 2.6 (A) A schematic of MFP-3D. In this device the sample is kept on lateral scanner (XY positioning stage) which is a piezo actuated flexure stage. The motion in vertical direction is provided to the head which houses the cantilever and the detection system comprising of the laser and the photodiode. This motion is provided by the piezo actuated z -positioner. The photodiode output which measures the cantilever deflection is utilized by the control design to obtain set point regulation and to prescribe profile estimate signal. (B) A Schematic of control implementation on DSP. The deflection signal from photodiode is sampled at 5 MHz and is used by the control algorithm in the DSP. The control signal generated by the DSP is then amplified and fed into the Z-piezo.

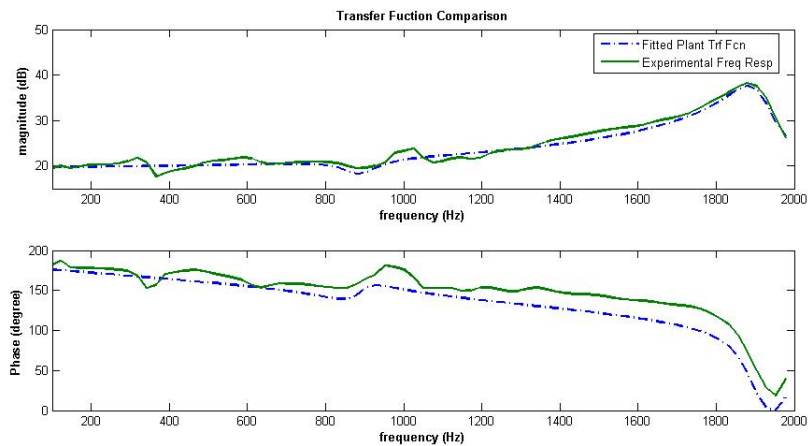


Figure 2.7 A comparison of experimentally (solid) obtained and fitted (dotted) frequency responses of the plant G .

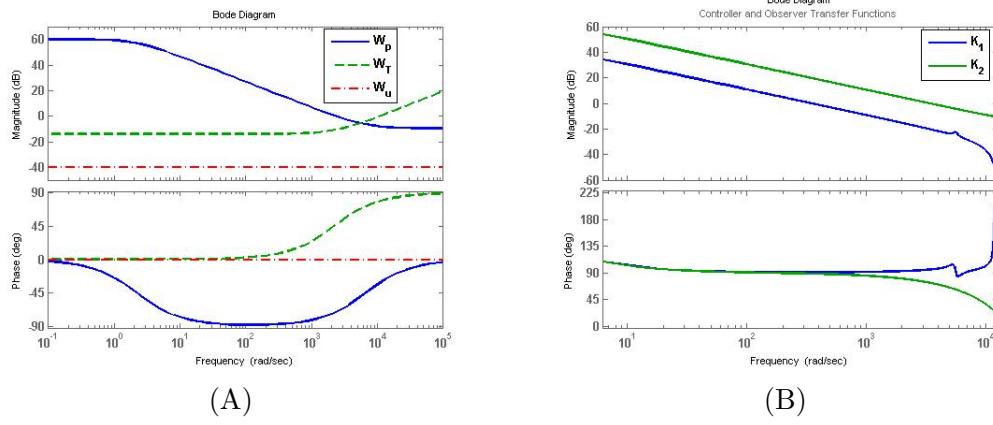


Figure 2.8 Control Design: (A) Weighting function for Sensitivity, Complementary Sensitivity and Actuation signal (W_S , W_T and W_u) respectively (B) Transfer functions of controller K_1 and observer K_2 obtained from *hinf*syn design.

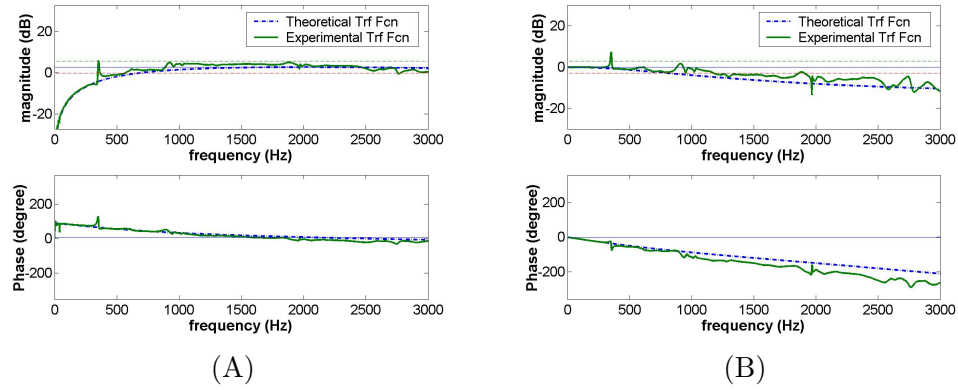


Figure 2.9 Experimental validation: (A) and (B) The plot compares the simulated and the experimentally obtained sensitivity and complementary transfer functions respectively. There is a good match between the two.

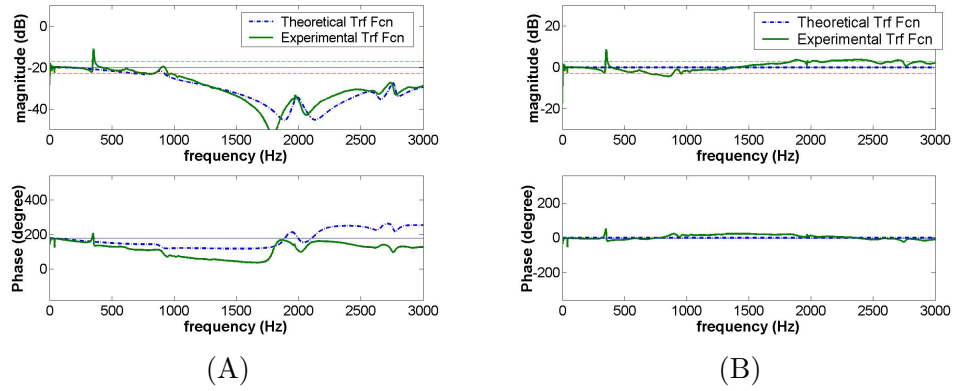


Figure 2.10 (A) The experimental frequency response of the control effort u to sample topography illustrates that it is not a good estimate of topography at high frequencies (B) The experimental frequency response of the estimate \hat{d} to sample topography remains flat corroborating the analytical result that this transfer function is a constant - the magnitude plot is within ± 3 dB and the phase is near zero over the entire range.

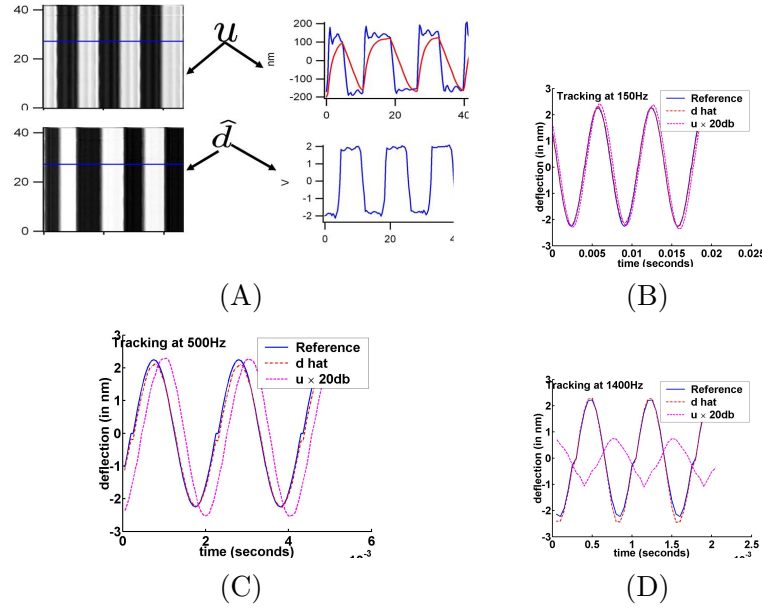


Figure 2.11 (A) Experimental data shows that significantly superior images (left panel) are obtained by using the new imaging signal \hat{d} when compared to the existing use of the control effort u as the sample topography estimate. (B,C): The plots show that the u signal gives worse estimates as the frequency of the d is increased (150 Hz and 500 Hz). The magnitude plots are consistent but there is a considerable phase lag. The \hat{d} signal on the other hand has practically no phase lag. (D) Experimental data that shows that the new imaging signal \hat{d} follows a 1.4 KHz reference sine wave that the control signal is unable to track at all.

CHAPTER 3. SYSTEMS SOLUTION TO FUNDAMENTAL LIMITATION IN IMAGE RELIABILITY IN INTERMITTENT MODE PROFILE ESTIMATION

In previous chapter a systems approach has been presented to mitigate the limitation on scanning bandwidth imposed by vertical scanner dynamics in contact mode imaging. However, cantilever dynamics is one of the limiting factors in imaging reliability and bandwidth in intermittent contact mode (also known as dynamic mode and Tapping mode AFM (TM-AFM) imaging. Conventional dynamic mode AFM imaging depends on steady state amplitude and phase of the cantilever for reconstructing the surface profile. Dependence on steady state parameters makes dynamic mode AFM imaging vulnerable to inaccuracies during transient state of the cantilever. In contact mode imaging, cantilever dynamics is rarely excited and therefore cantilever dynamics does not play major role in generating imaging artifacts. On the contrary, in dynamic mode AFM imaging knowledge of cantilever dynamics and transient behavior is essential to distinguish imaging artifacts from actual sample profiles.

Even though cantilever is well modeled by a spring-mass-damper system during free oscillation, its behavior gets complicated when it interacts with the sample surface. Highly non-linear, non-monotonic and unknown tip-sample interaction forces, periodic interaction between tip and sample and presence of unmodeled RHP zero complicates the response of the cantilever in dynamic mode AFM imaging. While physics community has made significant

effort to estimate cantilever behavior and imaging artifacts by applying first principle modeling, most of the cases the solutions are approximate and too complicated to be considered for real-time application.

Coupled with the physical complexity, availability of processing power raises unsurmountable challenge in accurate dynamic mode AFM imaging. Considering typical cantilever in dynamic mode AFM imaging may operate anywhere between 10KHz to 1MHz, even a 20 point per cycle sampling mandates 200KHz to 20MHz sampling speed and commensurate processing power. Recent trend of digital circuitry and high-frequency cantilever underscores the stated issue even more - so in future we may expect cantilever dynamics will become a more and more limiting factor in dynamic mode AFM imaging.

The limitation imposed by the cantilever dynamics may be broadly separated in two categories: reliability and bandwidth. While a multitude of solution has been proposed to address the bandwidth, reliability has never been addressed. Since all imaging schemes in dynamic mode AFM imaging relies on steady-state response of the cantilever, they are ineffective during transient of the cantilever. Not only that, these methods can not differentiate between the transient and steady-state behavior of the cantilever. As a result, even during the transient state of the cantilever, dynamic mode AFM imaging schemes keep reconstructing surface profile following the steady-state imaging principle: therefore generating spurious images as explained in Section 3.2.

Most bandwidth enhancing schemes try to suppress the transient behavior of the cantilever by modifying cantilever response by changing physical structure or electronic feedback. However, since these schemes can not separate transient behavior from steady-state one, they continue to apply same modifications even when the cantilever is in steady-state. This blanket

approach has a detrimental effect on steady-state image quality (e.g. lowering Q of cantilever reduces force sensitivity). Hence it is mandatory to identify the transient mode of the cantilever before applying any scheme to modify transient behavior of the cantilever. First step toward that will be to identify the areas of the image where cantilever is generating spurious images due to its dynamics. In this chapter, a novel model-based approach is developed to determine regions of dynamic atomic force microscopy based image where the cantilever fails to be an effective probe of the sample. It is experimentally shown that conventional imaging signals like the amplitude signal and the control signal that regulates the tip-sample separation may lead to ambiguous interpretation of the image. A quantitative measure called reliability index, is proposed as diagnostic measure for determining probe-loss. It is experimentally demonstrated that probe-loss affected portion of the image can be unambiguously identified the reliability index signal that can be determined in real-time.

3.1 Introduction

In dynamic mode operation of the atomic force microscope (AFM), the base of the cantilever is forced sinusoidally near the first modal frequency of the cantilever. When the cantilever tip interacts with the sample, the tip-sample interaction force changes the deflection of cantilever. The sample features are gleaned from the cantilever deflection signal. In amplitude modulated AFM (AM-AFM) operation[1](also known as tapping mode AFM), the amplitude of the first harmonic component of the cantilever oscillation is regulated at a desired set point by maintaining a constant tip-sample separation.

In tapping mode AFM, vertical piezo actuation signal that regulates cantilever-sample separation is interpreted as the image of the sample[1]. In a less prevalent mode, namely

Modified from a paper published in *Applied Physics Letters*[35]

error signal mode (ESM) imaging, feedback loop serves as a high-pass filter and error signal that is the difference between the cantilever amplitude and the setpoint amplitude[36] forms the image of the sample.

3.2 Source of spurious image

The cantilever is the only sensor for sample topography and therefore when the cantilever loses its interaction with the sample, it is not possible to glean any information about the sample from the cantilever deflection. We will term the condition of the cantilever not being affected by the sample as the probe-loss condition. All existing dynamic imaging methods suffer from the fundamental drawback of their inability to identify probe-loss affected regions of an image.

A good discussion of spuriousness in AFM images can be found in prior works[37], where probe-loss and tip-effect are shown to be the main contributors to spuriousness. Effect of probe-loss becomes a fundamental limitation when imaging at speeds where scanner bandwidth no longer limits the imaging speed [38] or the system operates in open loop [39]. All prior works have attempted to address the issue of probe ineffectiveness without identifying the occurrence of probe-loss. Issue of low imaging bandwidth and probe-loss due to transient response of probe has been partially addressed by active Q control of probe[40, 37]. Q control is widely accepted as solution for improving cantilever response. However overall reduction of Q , that reduces probe-loss affected region, has unwanted on-sample behavior that include lower vertical resolution and higher forces on sample[41]. Even though proposed methods reduced the areas of spurious image, fundamental problem of identifying the probe-loss has remained unanswered.

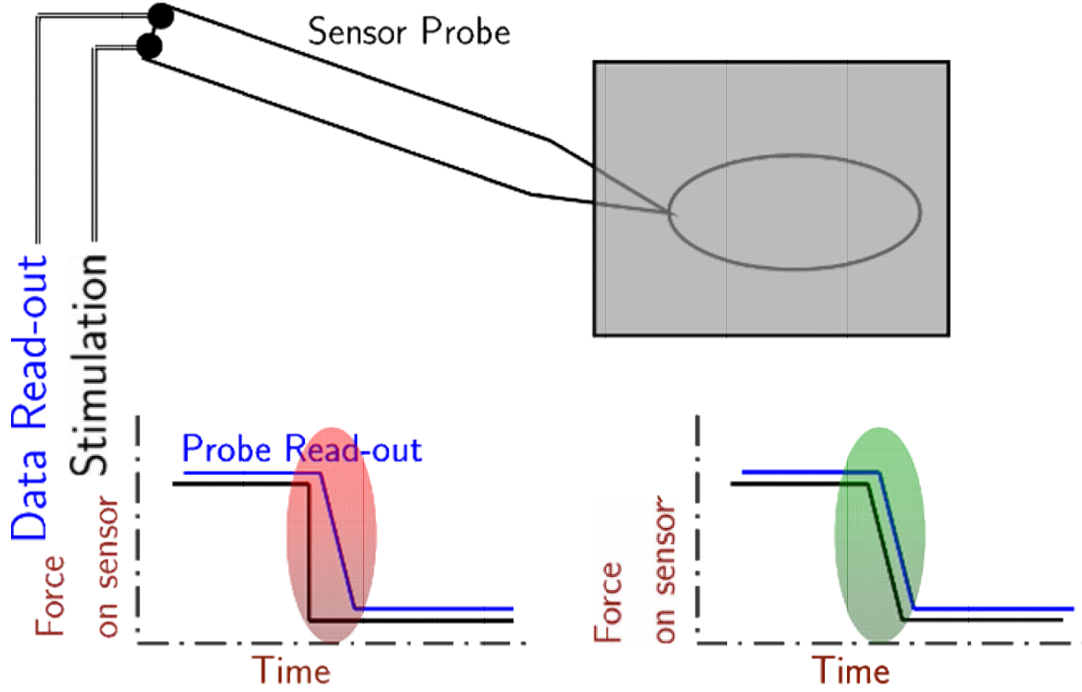


Figure 3.1 Steady state based imaging schemes can not differentiate between two different sample surfaces. As demonstrated in the figure, the AFM generates identical imaging signal for two different surfaces. In the left hand side, the cantilever is scanning a steep vertical surface. When the cantilever encounters the vertical wedge, due to high quality factor it takes typically $\frac{f_0}{Q}$ cycles to reach the steady state, where f_0 is the resonant frequency of the cantilever and Q is the quality factor. During this time, vertical scanner extends to reach the cantilever tip at a rate governed by the gain of the controller. Till it regains contact with the tip, actuation signal to the vertical scanner (u) does not represent the actual surface profile. This is evident from the schematic: where the surface reconstruction depending on the u signal creates a non-vertical wedge. On the other hand, when the surface is indeed a non-vertical one, the scanner could always keep the cantilever in contact with the surface, thereby creating a true reproduction of sample profile.



Figure 3.2 Experimental demonstration of probe-loss: A square grating (dotted-line) is imaged in dynamic mode. As the cantilever comes off the surface, a spurious image (solid-line; a trapezoidal shape) is generated.

3.3 Experimental demonstration of sensor loss

Problem of identifying spurious image due to probe-loss has remained untackled till now because the traditionally employed signals that estimate the sample features are not characteristically different in presence or absence of the probe-loss condition. This leads to erroneous interpretation of images and data, where a probe-loss condition is often interpreted as a manifestation of a sample feature.

Vulnerability of dynamic mode AFM operation to probe-loss is evident in Figure 3.3(a) and 3.3(b) that present images of uniform rectangular and triangular sample profiles respectively. Samples are scanned at 20 Hz spatial frequency by a Multimode AFM, manufactured by Veeco Metrology Inc. A silicon cantilever with resonant frequency $f_0 = 71.3 \text{ kHz}$ and quality factor $Q = 124$ was used in these scans. For convenience of presentation, all signals are shifted and

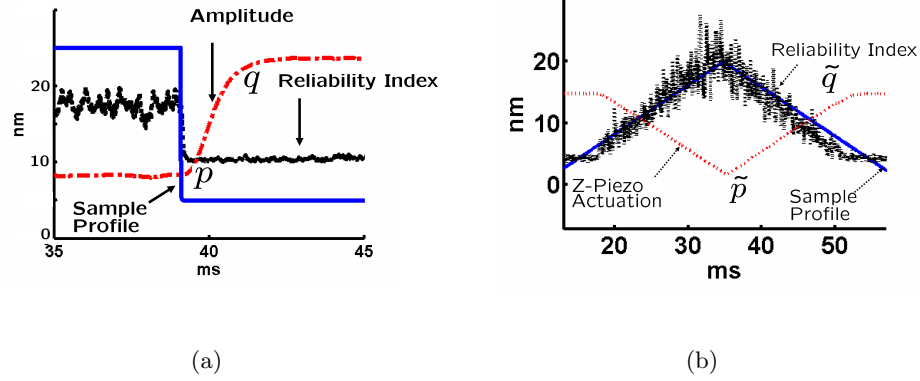


Figure 3.3 Shows the experimentally obtained amplitude signal during ES-M-AFM imaging. (a) and (b) shows the amplitude profile and reliability index when imaging a rectangular and triangular sample respectively.

scaled by appropriate constant.

Figure 3.3 demonstrates experimentally that similar amplitude profiles can result when the cantilever is probing two different sample profiles. In Figure 3.3(a), at p the sample has a step feature where the cantilever stops interacting with the sample leading to probe-loss. The amplitude increases slowly till it attains its free resonant amplitude at q . In Figure 3.3(b) the cantilever probe is active throughout the imaging region and the image is not affected with probe-loss. Amplitude profiles are similar between p and q and between \tilde{p} and \tilde{q} , even though two different samples are being probed. Therefore amplitude or error signal is not a reliable imaging parameter. Images generated in TM-AFM also lead to ambiguous interpretation due to probe-loss. Figure 3.4(a) and Figure 3.4(b) show tapping mode images of rectangular and triangular profiles at 20 Hz respectively. In Figure 3.4(a) height profile displays a smooth transition instead of a sharp edge. The height profile generated while going down the ramp between \tilde{p} and \tilde{q} in Figure 3.4(b) is similar to probe-loss region between \hat{p} and \hat{q} in Figure 3.4(a). It demonstrates that vertical actuation signal is also not well-suited as a measure of probe-loss.

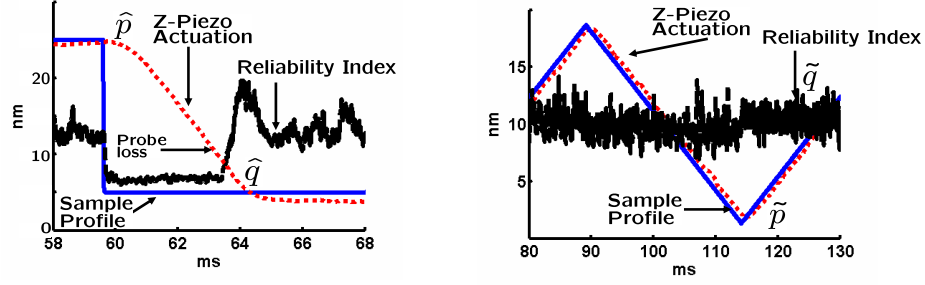


Figure 3.4 Shows the experimental vertical piezo actuation signals during TM-AFM imaging. (a) and (b) shows the height profile based on vertical actuation signal when imaging a rectangular and triangular sample respectively.

3.4 Detection of probe loss

It is apparent from the above two illustrative experiments that the amplitude and the vertical actuation signal may lead to ambiguous interpretation of data where it is not possible to distinguish between two different sample profiles. There is thus an evident need to identify the probe-loss scenario so that the AFM data can be interpreted correctly. In this chapter, a method for detecting probe-loss during imaging is presented. It is also shown that the method can detect the probe-loss situation fast enough that enables its use in real-time to minimize the probe-loss affected region.

3.5 Cantilever dynamics and observer

Near its first resonant frequency, cantilever can be mathematically modeled as a spring-mass-damper system [42]. In absence of the sample, cantilever-tip dynamics can be described by the following equation of motion:

$$\ddot{p} + \frac{\omega_0}{Q}\dot{p} + \omega_0^2 p = g(t) + \eta(t); [p(0), \dot{p}(0)] \quad (3.1)$$

where $\omega_0 = 2\pi f_0$ is first resonant frequency of cantilever, Q is quality factor of the cantilever, p is cantilever deflection, $p(0)$ is initial tip deflection, $\dot{p}(0)$ is initial tip velocity, $g(t)$ is dither forcing and $\eta(t)$ is thermal noise. Tip position of the cantilever is detected by the photo-diode that generates voltage $y = Sp + v$ where S is photo-diode sensitivity and v is measurement noise. With these parameters, the cantilever dynamics can be mimicked by an analog circuit or by a fast digital architecture called the observer of the cantilever. The observer output voltage, \hat{y} , follows the dynamics given by:

$$\ddot{\hat{y}} + \frac{\omega_0}{Q}\dot{\hat{y}} + \omega_0^2\hat{y} = g(t), [\dot{\hat{y}}(0), \hat{y}(0)] \quad (3.2)$$

where $\hat{y}(0)$ and $\dot{\hat{y}}(0)$ form the initial conditions of the observer state. In proposed scheme, a correction signal ($u(t) = [l_1 \ l_2]^T [e(t) \ \dot{e}(t)]$) is added to $g(t)$ and given as input to observer circuit to make observer track the cantilever faster (effectively decoupled from Q), where $e := y - \hat{y}$ (called *innovation* here after) is the difference between the cantilever deflection and the observer estimated deflection and $L = [l_1 \ l_2]^T$ is the gain of the observer. When the cantilever is not interacting with the sample innovation follows the equation:

$$\begin{aligned} \ddot{e} + \left(\frac{\omega_0}{Q} + l_1\right)\dot{e} + \left(\omega_0^2 + \frac{\omega_0}{Q}l_1 + l_2\right)e = \\ \eta - l_1\dot{v} - \left(\frac{\omega_0}{Q} + l_1\right)v; [e(0) \ \dot{e}(0)]. \end{aligned} \quad (3.3)$$

3.6 Model mismatch

In the absence of the sample, in steady-state, the error e is near zero as the cantilever dynamics given by (3.1) and the observer dynamics given by (3.2) are identical. The remnant mismatch in this case is due to photo-diode noise and the thermal noise that forces the cantilever. In the presence of the sample, the cantilever behaves as a modified cantilever with changed stiffness and changed resonant frequency. If the sample force is given by $h(p, \dot{p})$, the

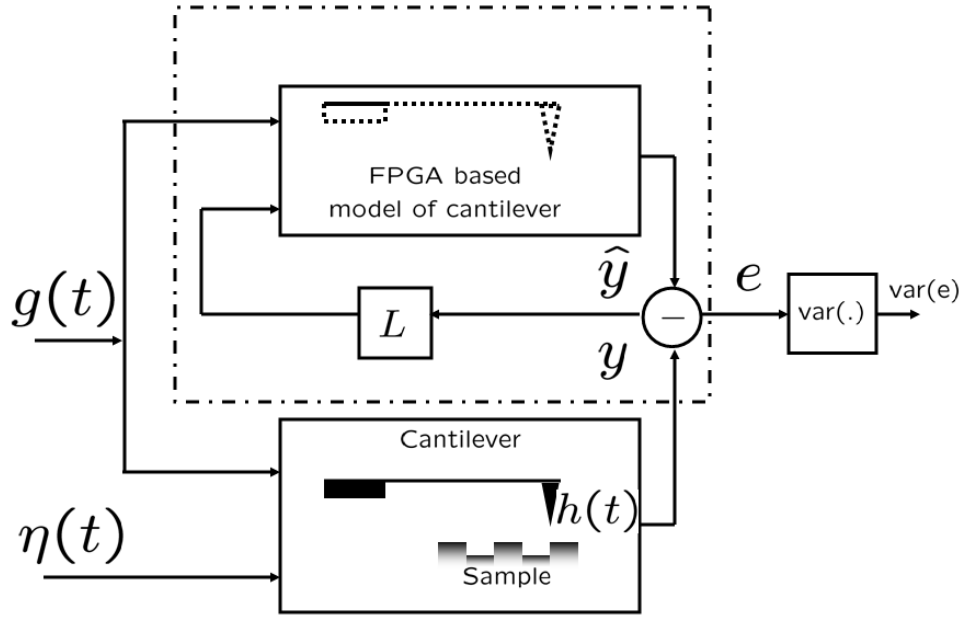


Figure 3.5 Model of the cantilever near its resonant frequency is mimicked by a high speed (10 MHz) electrical circuit implemented on Xilinx Virtex II Pro XC2VPX30 FPGA. Non-zero value of e arises from initial condition mismatch, $\eta(t)$ and $h(p, \dot{p})$.

estimate of the change in cantilever frequency and quality factor is given by[43, 44]:

$$\omega_0'^2 = \omega_0^2 + \frac{2}{a} \frac{1}{2\pi} \int_0^{2\pi} h(a \cos \psi, -a\omega \sin \psi) \cos \psi d\psi \quad (3.4)$$

and

$$\frac{\omega_0'}{Q'} = \frac{\omega_0}{Q} + \left(\frac{1}{a\omega} \frac{1}{\pi} \int_0^{2\pi} h(a \cos \psi, -a\omega \sin \psi) \sin \psi d\psi \right), \quad (3.5)$$

where a is the steady state amplitude of the cantilever in the presence of the sample. Thus the cantilever behavior under the sample presence is given by:

$$\ddot{p} + \frac{\omega_0'}{Q'} \dot{p} + \omega_0'^2 p = g(t) + \eta(t). \quad (3.6)$$

Note that the observer still behaves according to (3.2), thus the difference between the observer and the cantilever is due to the change in the model parameters, that do not decay with time. This is unlike and in stark contrast to the change due to initial condition mismatch caused by an impulsive force which is erased by observer in a couple of oscillations[45]. Probe-loss scenario demands a method to detect a persistent presence (or absence) of the sample. Effect of initial condition mismatch in innovation signal decays within a couple of cycles. Thus the observer could potentially track the cantilever even on the sample, had there been no mismatch in parameters. However, in presence of sample, due to change in effective cantilever parameters we observe a persistent non-zero innovation signal. As soon as sample is removed, the cantilever behaves according to its original parameters and the innovation recovers near zero value in a couple of cycles. To utilize this property of innovation, a new parameter, called reliability index (N sample variance of innovation, where N is chosen according to observer bandwidth, false alarm and miss probability in probe-loss detection), is derived which maintains a high value when tip is interacting with sample and drops to near zero value otherwise. In Figure 3.3(b), it is evident that reliability index increases monotonically with decreasing tip-sample separation. This result agrees with the intuition that smaller tip-sample separation

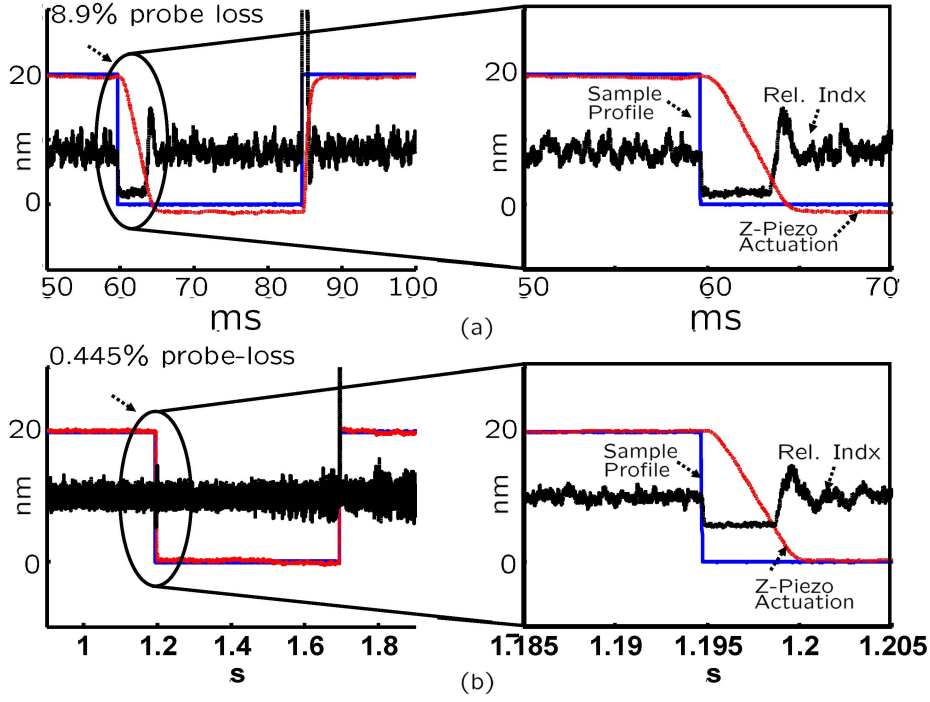


Figure 3.6 In (a) and (b), a rectangular profile is imaged at 20 Hz and 1Hz respectively.

leads to greater changes to equivalent resonance frequency and equivalent damping, thereby leading to greater model mismatch between observer and cantilever dynamics. This property of reliability index immediately lends itself for design of thresholds for detection of probe-loss. In Figure 3.3(a) reliability index drops below threshold (equivalent to $10.0nm^{\dagger}$) within couple of cycles as it comes off the step indicating detection probe-loss condition. As a comparison, amplitude signal takes approximately 155 cycles to indicate that cantilever is no longer interacting with the sample. In Figure 3.4, reliability index is used for detection of probe-loss and spurious image, which is not possible using traditional imaging parameters like amplitude(A), error signal($A - A_{setpoint}$) or vertical piezo actuation signal. Figure 3.4(a) shows that when the cantilever comes off the step at \hat{p} the reliability index drops only in a couple of

[†]From definition, reliability index is a dimensionless quantity. However, for demonstration purpose it has been plotted on same scale of amplitude and height

cantilever oscillations, indicating spurious image between \hat{p} and \hat{q} . At \hat{q} , height image becomes true reflection of sample profile and reliability index jumps above threshold, indicating end of probe-loss condition. In Figure 3.4(b) the reliability index stays above the threshold indicating that there is no probe-loss. It is to be noted that while in lower scan rate, effect of probe-loss is not so prominent, it is present for exact same duration as for any other rate. At 20 Hz scan rate 8.9% area contains spurious height profile as compared to 0.445% at 1 Hz scan rate. Even though, probe-loss is not very prominent in Figure 3.6(b), it is present for exactly same duration (4.45ms) as in Figure 3.6(a). The number of cycles of probe-loss is determined largely by the quality factor Q of the cantilever and is independent of the scan-rate, therefore creating more fraction of spurious image for higher scan speeds.

3.7 Conclusion

In this chapter, it is demonstrated experimentally that probe-loss is a fundamental limitation on image accuracy and imaging speed. Magnitude of reliability index, an new signal, is presented as a fast real-time quantitative measure to detect probe-loss and to identify reliable areas of an image. Because of monotonic dependence of reliability index on tip-sample separation, thresholds can be designed to trigger probe-loss detection with asserted level of confidence. As the probe-loss detection is done in real-time, it can be used as a signal that can be employed by the controller to take corrective action to minimize the probe-loss affected region. This is part of ongoing work.

CHAPTER 4. QUANTITATIVE STUDY OF YEAST MORPHOLOGY

AFM is widely used for studying surface morphology and growth of live cells. Although it is widely used for imaging live animal cells, there are relatively fewer reports on AFM imaging of yeast cells ([23], [24]). Yeasts have thick and mechanically strong cell walls and therefore difficult to attach to a solid substrate. In this report, a new immobilization technique for quantitative imaging and topographic characterization of living yeast cells in solid media using Atomic force microscope (AFM) is presented. Unlike previous techniques, proposed technique allows almost complete cell surface to be exposed to environment and studied using AFM. Apart from the new immobilization protocol, in this report, for the first time, high resolution height imaging of live yeast cell surface in intermittent contact mode is presented. Stable and reproducible imaging over 10 hour time span is observed. High resolution imaging and significant improvement in operational stability facilitated investigation of growth patterns and evolution of surface morphology in quantitative terms. Growth rate of mother cell and budding cell showed distinct patterns over the imaging time. Reliable quantitative data was collected for cell surface roughness. There is a strong motivation of determining evolution of cell surface morphology to study effect of cell aging on cell surface and this report is a significant step toward this challenging objective. Cell walls play a crucial role in biophysical processes in cells as the interface between the intra-cellular material and environment. Fungal cell walls are composed of complex network of proteins and polysaccharides. In general, genetic

and chemical methods are used to provide insights into formation, control and function of cell walls[46]. However, cell wall structure is a highly dynamic structure, changing constantly during cell division and growth. Real-time study of cell wall properties can provide new information about the evolution of cell wall morphology. *Saccharomyces cerevisiae* has been established as a convenient system for studying plant cell walls due to its robustness, short half life and well-characterized collection of mutants. Even though *Saccharomyces cerevisiae* is only one species of 1500 strong family of yeasts, it is the most common one and in subsequent section we have used the terms *Saccharomyces cerevisiae* and yeast interchangeably.

Main factors that governs the biosynthesis of plant cell wall are pre-existing cell wall structure, environmental conditions and genetic information. As a model eukaryotic cell, functions of enzymes and the mechanisms that regulate enzyme activity in *Saccharomyces cerevisiae* are well documented [47]. In addition, availability of the complete yeast genome sequence, has facilitated genetic manipulation of *Saccharomyces cerevisiae* . This makes yeast a good stepping stone toward AFM study of plant cell walls since effect of variety of genetic and enzymatic expressions on morphogenesis can be studied in real time.

Knowledge of the signaling pathways which leads to cell wall formation enabled scientists to selectively disrupt the pathways of these genes and affect cell wall composition and morphology. However, the effect of the genetic expression on ultrastructure of cell walls are yet to be studied. Even though structures of component macromolecules are well studied, architecture of cell wall is yet to be understood and molecular level information of cell walls will have a definitive impact in this direction. Electron microscopy and fluorescence tagging have been widely used for deciphering cell wall structures [48]. Molecular level information of cell walls will have a definitive impact in this direction and AFM can play an important tool

for unraveling cell wall structure. Atomic Force Microscopy is a new entrant in the field of analyzing biophysical factors affecting cell wall morphology and formation. Besides creating topographic images, AFM enables us to probe both physiochemical and mechanical properties of cell surfaces on a nanometer scale. AFM offers new set of tools to measure surface properties of yeast cell (and other cells alike) which are inaccessible to aggregate studies commonly used in biological investigation. AFM is an enabling technology for single cell investigation with unprecedented spatial resolution and direct measurement of surface material properties. Real time imaging provides a way to monitor cell surface dynamics during cell growth and to monitor effects of chemicals and environmental stresses, like osmotic pressure, temperature, and anti-fungal drugs. Compared to typical methods of cell wall characterization (for instance: chemical analysis of cell wall extracts, binding studies, digesting by enzymes and electrophoretic measurements), AFM studies do not require prior cell manipulation or averaging over ensemble of cells. AFM provides complementary information to traditional invasive and statistical methods by enabling study in native environment at single cell level.

4.1 Role of AFM in cell wall characterization

Deciphering functions of cell surfaces requires knowledge of their structural and physical properties. Electron microscopy has been the key tool for understanding cell surface ultrastructure. However, in last decade atomic force microscopy provides a powerful tool to investigate cell surfaces with angstrom resolution. AFM provides images of the surface ultrastructure in real time under physiological conditions. AFM may be used for force measurements, measuring molecular interactions, hydrophobicity, surface charges, surface properties (adhesion, stiffness), measurement of turgor pressure inside the cell[49], mapping cell wall texture and

composition and mechanical properties. These new metrics for cell wall characterization may provide new insight into the structure-function relationships of microbial surfaces. Chemically functionalized probes are used in [50] to investigate the surface charges of yeast cells, which play vital role in cell aggregation and drug delivery.

The introduction of the atomic force microscope (AFM) and its application to biological surfaces has offered new possibilities to obtain microscopic physiochemical properties of cell surfaces[51]. Besides metrology, AFM probes can be utilized as external mechanical indenter and models are developed for measurement of cell membrane tension and internal osmotic pressure[52]. Atomic resolution of AFM has assisted scientists to study ultrastructure of live yeast which are not visible by optical microscopes. Typical structures on yeast cell wall are in the scale of 2nm, which is not accessible by optical microscopes. Ability of imaging live cells in physiological condition opens up the possibility of studying real time evolution of cell wall structure.

4.1.1 Sample preparation for AFM

First successful attempt of immobilizing live yeast cells were done in 1995 - [24]. Cells were gently immobilized on 3% agar and submerged in culture medium, were imaged in contact mode with an atomic force microscope for 6-7 h. We may term the proposed method as reverse agar plating, because in this method a drop of molten agar is placed on yeast solution and as the agar solidifies, yeasts get trapped in the agar. Confocal microscopy confirmed that most of the cells do not travel deep in the agar surface and hence agar plate can be flipped upside down and trapped cells may be imaged by AFM. However, this method poses few challenges for proper imaging: molten agar introduces a heat shock for yeast since below 30 degree Celsius, viscosity of agar gel increases fast leading to an uneven spread, or flow from pipette. Also,

only a very small area of yeast surface gets exposed to AFM tip and nutrients. Contact mode imaging causes easy tip contamination and sometimes displaces cells which are not tethered well in surface (e.g. budding cells).

An alternative trapping method by using polycarbonate membranes was introduced in 1995 [23]. In this method yeast solution was "filtered" via porous polycarbonate membrane in negative pressure. If cell diameter and pore diameter matches, the cells get trapped in pores. The membrane is then reversed and cells trapped on the membrane surface are imaged using AFM. However, the yield of trapping is significantly low. Not all pores are of equal size and cell sizes do vary considerably. Only a good match between the cell and pore sizes ensures proper trapping. Even when cells are trapped, they may get pushed out of the pore due to vertical force applied by the probe. Stiff trapping hinders lateral growth of the cells and young cells, which are significantly smaller than pore size, can not be trapped resulting to the fact that trapped cells do not represent the actual cell population.

Several different other methods of immobilization exist; notably air drying [53], chemical immobilization [54], adsorption on silica surface [54]. However, all of these methods have irreversible effect on cell morphology, viability and metabolism. Hence, these methods are not suitable for investigation of cells in their native environment.

4.1.2 Study of cell morphology

There is a growing interest in establishing correlation between AFM evaluated morphological properties to intra-cellular processes. This requires quantitative measurement of morphological properties and establishing correlation with metabolic processes. It is reported that osmolarity and sodium azide concentration has significant effect on cell viability and cell surface elasticity [55]. In this direction, we propose new method of cell immobilization which

enables us to quantitatively image surface profile of yeast cells and analyze trends in surface roughness change with time.

As it is elucidated in section 4.2.2, immobilization of yeast cells for AFM imaging is one of the main challenges faced by researchers. Where none of the existing methods are perfect, membrane based trapping has gained wide acceptance due to its firm grip on cells when there is a successful trapping of cell (which is not a routine event and requires significant number of trials). In this work, we developed a new immobilization method where we relied on the natural process of growing yeast culture on solid media. It utilizes the fact that when yeasts are grown on solid media with nutrients, newly grown cells are well anchored to the media and so are the mature live cells which absorb nutrients from the media. Experimental data shows that this method is well suited for AFM imaging and provided extraordinary stable anchoring of live cells. Also, we obtained quantitative image of *Saccharomyces cerevisiae* cells in intermittent mode imaging; which is an enabling step toward high-resolution noninvasive imaging of live cells.

4.2 Protocol for immobilization of live *Saccharomyces cerevisiae* cells for AFM imaging

4.2.1 Inoculation of yeast culture

A budding yeast, *Saccharomyces cerevisiae* (YM4271, Clontech Laboratories, USA) was used in this study. An overnight saturated culture of YM4271 cells was diluted ten times and grown at 30°C under continuous shaking. Cells were collected at the logarithmic phase of growth by centrifugation at 1000×G for five minutes. The cells were then resuspended in one fourth the original volume with distilled water. About 100 μ l of molten YPD media containing

1.5 % Phytagar was dropped over a #1 thickness cover slip. Another cover slip was then placed over the agar surface and allowed to solidify. The top cover slip was gently removed and $5\mu\text{l}$ of yeast suspension was dropped on the agar surface. A new cover slip was placed over the cells and allowed to incubate at 30°C for 3 hr prior to AFM observations. Subsequently cells are imaged using an AFM which has significantly higher travel range ($15\mu\text{m}$) in vertical direction. To enhance the resolution and to be minimally invasive, a stiff cantilever is used in intermittent contact mode and images are recorded for consecutive 10 hours.

4.2.2 Prepare immobilized cells for AFM imaging

Once the yeasts are spotted on the agar surface, the glass slide is placed on a petridish and petridish is sealed with paraffin film to prevent desiccation of cells. The petridish is placed in incubator at 30°C for 30-45 minutes. However, it may be necessary to increase incubation time up to 3 hours in some cases (when cells are growing slowly, e.g. after treating with sodium azide). After incubation is complete, the glass slides are placed under airflow for brief amount of time (typically 10 minutes or less) to remove surface moisture. At the end of this process, the sample is ready for AFM imaging.

The yeast samples are imaged with MFP-3D, an AFM manufactured by Asylum Research, Santa Barbara, CA in intermittent contact mode. We used AC240 Silicon Cantilevers, manufactured by Olympus, with approximate spring constant of 1 N/m and quality factor of 160. Typically, AFM gain settings are set at relatively high value, integral gain at 16–20 and proportional gain at 0–4. However, we need to be careful to adjust gains to a lower value if any oscillation or instability in feedback loop is observed. Typical free oscillation amplitude of the cantilever is 150–200nm and set point is set at 60–80% of free oscillation amplitude. Image resolution was found to be better when the set point is just below the point where image dis-

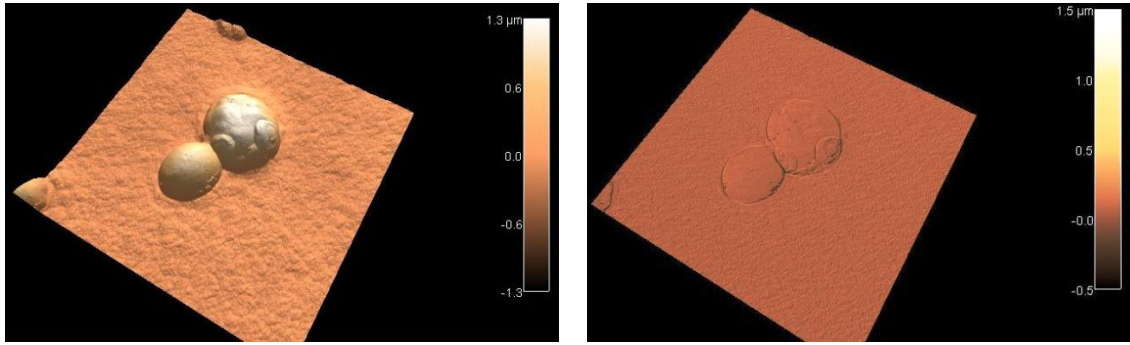
appears. However, to avoid effects of squeeze film, initial set point should be kept at 50–60% of free oscillation amplitude and then gradually increased till image disappears. After that set point is lowered again till the image re-appears. This ensures gentle imaging without the problem of false engagement and squeeze film.

All images are captured at 512×512 resolution, with tip velocity of approximately $2.5 \mu\text{m/s}$ to $5 \mu\text{m/s}$. The nanopositioning stage is moved in X and Y direction by a piezo actuated flexure in a feedback controlled closed loop with sub-nanometer lateral resolution. As the nanopositioning stage moves the sample for raster scan, the vertical feedback loop extends and contracts the vertical piezo to keep the amplitude of oscillation constant [1]. The difference between the set point amplitude and amplitude is demonstrated in Figure 4.2(b), which shows the sharp edges of the yeast surface.

4.3 Results and Discussion

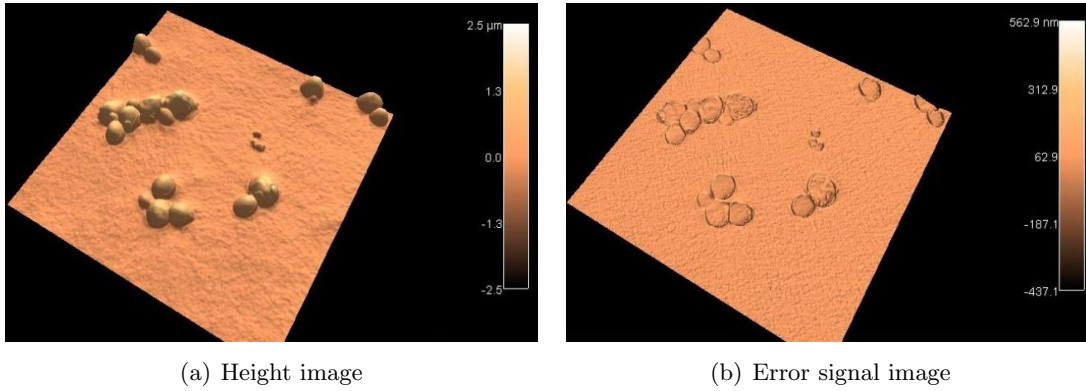
With above immobilization method and AFM settings, *Saccharomyces cerevisiae* samples were imaged for 10 hours without any degradation in image quality. Even though, some cells stopped growing after 6–8 hours, anchoring was firm enough to continue to image beyond that time frame. Figure 4.2(a) shows the image of live yeasts after 6 hours of imaging. Ultrastructure on the surface of mother cell can be clearly observed in Figure 4.1(a). In Figure 4.1(a), one may clearly observe the bud scar on the mother cell.

New immobilization method enabled us to trap the live cells in least invasive way and the complete cell was exposed to environment. This helps in more efficient absorption of nutrients and inhibitors as compared to existing methods. Since cells are grown on nutrient rich agar media, this method of immobilization is essentially same as streaking of yeast stocks



(a) Height image of *Saccharomyces cerevisiae* in nutrient rich Media (b) Error signal image of *Saccharomyces cerevisiae* in nutrient rich Media

Figure 4.1 *Saccharomyces cerevisiae* in nutrient rich Media



(a) Height image

(b) Error signal image

Figure 4.2 Multiple *Saccharomyces cerevisiae* cells in nutrient rich media

on agar and very close to natural growth environment for yeast colonies. New immobilization method eliminates uncertainties associated with membrane based immobilization and produces a uniform cell density over the agar surface where cells of all ages, sizes and shapes are accessible to AFM probe. In contrast to membrane based immobilization, this method allows us to investigate the daughter cells too, which have significantly different physiological properties as compared to the mother cells. As observed in Figure 4.1(a), both mother and daughter cells are imaged simultaneously, which is not possible in membrane based immobilization.

This method also offers advantages over reverse agar plating. In this new method, maximum cell surface is accessible to the probe and therefore a complete image of the cell is obtained. In

reverse agar based imaging, growth of neighboring cells affects the height image of each other due to stretching of agar film; a problem which is eliminated in the new method.

4.3.1 Significance of quantitative imaging

We obtained high resolution height mode images of live yeast cells using intermittent contact mode imaging. Most of the prior arts focus on contact mode imaging and relies on error mode imaging for visualizing ultrastructure. Given relatively large size of yeast cells, error mode imaging is not suitable for quantitative analysis of surface morphology since the probe-surface interaction encounters non-linearity and error signal does not vary linearly with surface features. Hence, the AFM images do not represent the true surface features quantitatively. In [53], intermittent contact mode has been used for air-dried cells, but viability of cells decreases significantly when the cells are dried on non-nutrient media (e.g. glass slide). In this report, ultrastructure are resolved in height mode images using intermittent contact mode, which enabled analysis of cell morphology quantitatively and observe real time evolution of surface features. Stable imaging condition allowed quantitative measurements of height and surface roughness of the *Saccharomyces cerevisiae* cells, as demonstrated in Section 4.3.2.

4.3.2 Study of cell morphology

In the study of cell morphology, we focus on cell height increase and roughness change. As we observe from the experimental results, both the mother and daughter cell increase in height with time, but rate of growth is higher in daughter cell (Figure 4.3). During first four hours of observation, daughter cell increased approximately 60% in diameter, whereas mother cell increased only 5%. This observation corroborates the existing knowledge that matured yeast cells are approximately $5\mu m$ in diameter. Since the mother cell under observation has attained

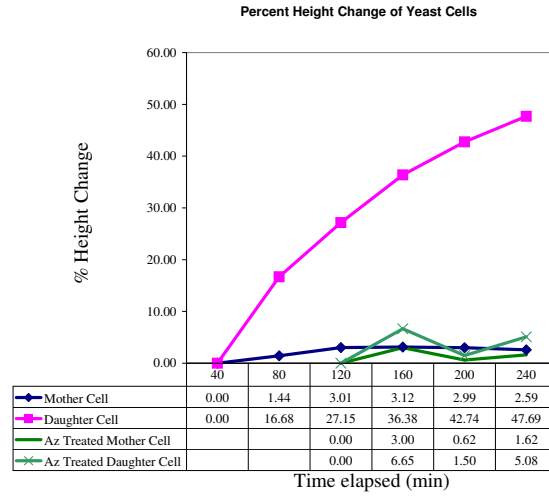


Figure 4.3 Percent Change in Yeast height

the maximum cell volume, it does not increase in height or diameter.

The roughness change of the cells under investigation is reported in Figure 4.4.

We observed different types of trends in roughness variation on cell wall: on mother cell, roughness does not change significantly or shows a very slow increase. On the other hand, on daughter cells, roughness decreases at a fast pace, holds steady for 1-2 hours and then increases slowly. It has to be noted that, different parts of same cell may show different behavior and we have to take average around the point of interest to obtain a statistically significant trend. As observed in the daughter cell, after achieving the minimum roughness, dynamics of roughness evolution follows the increasing trend similar to the mother cell. From Figure 4.4, it may be observed that roughness change of daughter cell (Point I) between last 40 minutes is similar to that of mother cell between first 40 minutes. For the data to be statistically significant, multiple square areas around each points were selected and roughness was averaged.

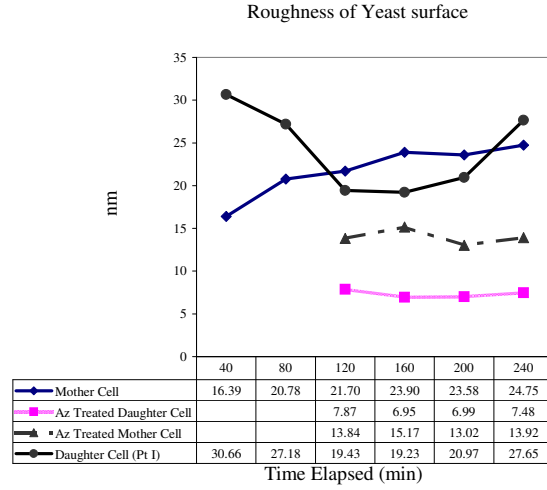
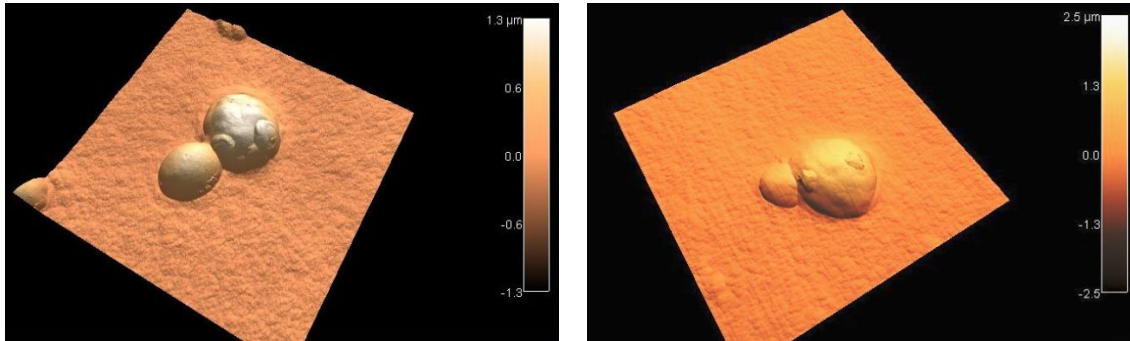


Figure 4.4 Roughness variation in yeast cell wall



(a) Height image of yeast in nutrient rich Media (b) Height image of Azide treated yeast in nutrient rich Media

Figure 4.5 Height image of yeast cells without and without growth inhibitor: even though both cell cluster is layered on nutrient rich media, non-azide treated cell shows growth and roughness change but Azide treated yeast does not demonstrate any consistent pattern in growth or roughness change. Also, height image demonstrated Azide treated yeast is structurally intact after Azide treatment, hence the inactivity is contributed to Azide treatment only.

4.3.3 Inhibition of growth and roughness variation by Sodium Azide treatment

To confirm observed trend in surface morphology is indeed an effect of cell metabolism, and not a manifestation of changes introduced by extra-cellular environment, a control experiment was performed. After immobilization, cells were treated with 50 mM Sodium Azide solution for 1 hour and then imaged using AFM. However, it may be noted that adhesion to the media is not as strong as before, probably attributed to the fact that cells no longer absorb nutrient from media. Sodium Azide stops the cell metabolic process without affecting the morphology of the cell wall (Figure 4.5). Azide stops the height evolution of yeast cells; the height fluctuates randomly within 5% of its original value in both mother cell and daughter cell which is in contrast with the untreated cells. The variation in roughness is minimal and statistically there exists no trend within 90% confidence level. This flatness rules out the possibility of non-metabolic effects on height or roughness variation previously observed in live cells.

4.4 Conclusion:

Proposed immobilization method is an enabling step toward quantitative imaging of live cells in intermittent contact mode. Stable anchoring and high resolution height mode imaging open new avenues for real-time study of surface properties. While this report associates roughness variation with cell metabolism, deciphering the exact mechanism of cell wall material deposition remains an open question. Future studies on mutants where PKC pathway has been blocked selectively may establish the correlation between cell wall material deposition and roughness.

CHAPTER 5. FUTURE WORK AND CONCLUSION

Scientists and engineers are constantly striving to unravel structure and dynamics in molecular level with the newly found powerful device called AFM. However, their abilities are limited by the complex dynamics of the instrument itself. Focus on speed of AFM operation often overshadows other fundamental requirements, e.g. reliability, robustness, repeatability and ease-of-use. In this work, we have presented new system based approaches to address these fundamental requirements.

Future work

Extending High-Bandwidth profile estimation to intermittent contact mode imaging:

In Chapter 2 we have presented model-based approach to achieve orders of magnitude improvement in imaging speed in contact mode. We also demonstrated that imaging speed is limited only by the accuracy of the frequency domain model of the vertical scanner. Therefore, this method can easily be extended to intermittent contact mode imaging, where amplitude of the cantilever is used for maintaining a constant tip-sample separation. If the cantilever is actuated using a constant frequency, the model of AFM can be derived considering vertical scanner actuation as input and cantilever amplitude as output. However, significant challenge remains to model the oscillating cantilever during tip-sample interaction. It has been demon-

strated in Section 3.5 that under periodic interaction with the sample, the cantilever can be modeled as an equivalent spring-mass-damper system with a right-hand zero. Using this model, we can extend the algorithm presented in Section 2.6 without any further modification, where G will represent the transfer function between vertical piezo actuation signal and output of the oscillating cantilever. Therefore, significantly high-bandwidth imaging may be achieved in intermittent contact mode imaging by deploying a model based approach.

Utilizing reliability index to increase imaging bandwidth in intermittent mode AFM imaging

It has been demonstrated in this work that images generated in TM-AFM lead to ambiguous interpretation due to sensor-loss. TM-AFM imaging can not determine the region of sensor-loss. During the time the cantilever loses contact, the feedback loop extends the piezo to come back into contact with the cantilever.

In one embodiment, the detection of the sensor-loss situation is fast enough to be of real-time use. In this work, we have presented a real-time measure to detect sensor-loss, called reliability index. Thus the method can be employed for correct interpretation of the image and can be used to minimize the sensor-loss affected region of the image by taking suitable corrective action. As and when sensor-loss is detected by reliability index, the quality factor of the cantilever can be dynamically lowered for quickly reach steady-state amplitude. This dynamic change of quality factor will eliminate issue of lower on-sample resolution associated with universal quality factor reduction. Besides improving cantilever's off-sample behavior, reliability index can be used to increase the response speed of the vertical piezo by dynamically adjusting gain of z-feedback loop. In most imaging efforts, gain can not be arbitrarily increased because of on-sample oscillatory behavior of feedback loop. However, reliability index may be

used to operate at two different gains on-sample and off-sample. This will ensure faster response in sensor loss affected areas and stable behavior in reliable imaging areas. Preliminary studies suggest that dynamic gain adjustment can significantly lower sensor loss affected areas and thereby can boost imaging speed in intermittent contact mode.

Unraveling correlation between morphology and metabolism

Proposed immobilization method is a significant step toward quantitative imaging of live cells in intermittent contact mode. Stable anchoring and high resolution height mode imaging open new avenues for real-time study of surface properties. While this report associates roughness variation with cell metabolism, deciphering the exact mechanism of cell wall material deposition remains an open question. Future studies on mutants where PKC pathway has been blocked selectively may establish the correlation between cell wall material deposition and roughness. Quantitative imaging is a definite step toward harnessing power of AFM to study the effect of nutrients and inhibitors on cell morphology.

Conclusion

We have presented systems approach to improve performance and reliability of AFM imaging. Prior knowledge of system dynamics have been used to increase imaging bandwidth in contact mode, without compromising with conventional imaging goals: set point regulation, noise rejection and minimizing actuation energy. It has been analytically demonstrated that if models are known accurately, proposed method can estimate sample topography with *zero error* at all relevant imaging speed. Also, we have addressed fundamental question of imaging reliability in intermittent contact mode imaging by using dynamic model of cantilever. For the first time, we implemented a high-speed digital circuitry to generate a real-time signal,

called reliability index, to detect sensor loss. Lastly, we proposed new method of anchoring live, round cells with stiff cell wall in nutrient rich media. Using this anchoring method, we successfully imaged live yeast cells intermittent contact mode. We successfully used height mode imaging to enable quantitative study of morphology.

CHAPTER 6. AREAS OF PUBLICATIONS

- Real-time detection of probe loss in atomic force microscopy [35] [56]
 - Real-time detection of probe loss in atomic force microscopy. Applied Physics Letters, 89(13): 133119 -, 2006
 - Real-time detection of probe loss in atomic force microscopy. Virtual Journal of Nanoscale Science & Technology, 14(15), October 9, 2006.
- Systems solution to the sample-profile estimation problem in atomic force microscopy [57] [58] [25]
 - Sample-profile estimate for fast atomic force microscopy. Applied Physics Letters, 87(5) :053112 -, 2005.
 - New approaches for sample-profile estimation for fast atomic force microscopy. volume 74 DSC, pages 1317 - 1326, Orlando, FL, United States, 2005.
 - A robust control based solution to the sample-profile estimation problem in fast atomic force microscopy. International Journal of Robust and Nonlinear Control, 15(16):821 - 837, 2005.
- Observer based imaging methods for atomic force microscopy [59]
 - Observer based imaging methods for atomic force microscopy. volume 2005, pages 1185 - 1190, Seville, Spain, 2005.

- Model development for piezo-actuated atomic force microscope stage [60] [61] [62] [63] [64] [65]
 - Model development for atomic force microscope stage mechanisms. SIAM Journal on Applied Mathematics, 66(6): 1998 - 2026, 2006.
 - Construction and experimental implementation of a model-based inverse filter to attenuate hysteresis in ferroelectric transducers. IEEE Transactions on Control Systems Technology, 14(6):1058 - 1069, 2006.
 - Experimental implementation of a model-based inverse filter to attenuate hysteresis in an atomic force microscope. volume 3, pages 3062 - 3067, Nassau, Bahamas, 2004
 - Model development and control design for high speed atomic force microscopy. volume 5383, pages 457 - 468, San Diego, CA, United States, 2004. Model development for piezoceramic nanopositioners. volume 3, pages 2638 - 2643, Maui, HI, United States, 2003
 - Model development and inverse compensator design for high speed nanopositioning. volume 4, pages 3652 - 3657, Las Vegas, NV, United States, 2002
- Micro-manipulation using combined optical tweezers and atomic force microscope [66]
 - Micro-manipulation using combined optical tweezers and atomic force microscope. Proceedings of SPIE, 6644:66441L, 2007.

BIBLIOGRAPHY

- [1] G. Binnig, C. F. Quate, and Ch. Gerber. Atomic force microscope. *Phys. Rev. Lett.*, 56(9):930–933, Mar 1986.
- [2] B. Bhushan. *Handbook of Micro/Nano Tribology*. CRC Press, 1995.
- [3] D. Bonnel. *Scanning Probe Microscopy and Spectroscopy: Theory, Techniques and Applications*. John Wiley & Sons, second edition, 2000.
- [4] JN Israelachvili. Intermolecular and Surface Forces. *Academic Press, London*, page 161, 1991.
- [5] M. Yves. *Scanning Probe Microscopes*. SPIE Press, 1995.
- [6] B.C. Crandall. *Nanotechnology: Molecular Speculation on Global Abundance*. MIT Press, 1996.
- [7] C.R.K. Marrian. *Special Issue on Nanometer-scale Science and Technology*, volume 85 of 4. Proceedings of the IEEE, April 1997.
- [8] G.M. Whitesides and H.C. Love. The art of building small. *Scientific American*, 285(3):39–47, September 2001.
- [9] M. Sitti and H. Hashimoto. Tele-Nanorobotics using Atomic Force Microscope as a Robot and Sensor. *Advanced Robotics*, 13(4):417–36, 1999.

- [10] A. Sebastian, M.V. Salapaka, D.J. Chen, and J.P. Cleveland. Harmonic and Power balance tools for tapping-mode AFM. *Journal of Applied Physics*, 89(11):6473–80, June 2001.
- [11] S-I Lee, S. Howell, A. Raman, and R Reifenberger. Nonlinear dynamics of microcantilevers in tapping mode atomic force microscopy- comparison between theory and experiment. *Physical Review B*, 66(11), 2002.
- [12] M. Ashhab, M.V. Salapaka, M. Dahleh, and I. Mezic. Dynamical analysis and control of micro-cantilevers. *Automatica*, 35(10):1663–70, October 1999.
- [13] S. Salapaka, M. Dahleh, and I. Mezic. On the dynamics of a harmonic oscillator undergoing impacts with a vibrating platform. *Nonlinear Dynamics*, 24:333–358, December 2001.
- [14] M.V. Salapaka, H.S. Bergh, J. Lai, A. Majumdar, and E. McFarland. Multimode noise analysis of cantilevers for scanning probe microscopy. *Journal of Applied Physics*, 81(6):2480–87, 1997.
- [15] G. Schitter, P. Menold, H. F. Knapp, F. Allgower, and A. Stemmer. High performance feedback for fast scanning atomic force microscopes. *Review of Scientific Instruments*, 72(8):3320–3327, August 2001.
- [16] A. Sebastian, J.P. Cleveland, and M.V. Salapaka. Robust control approach to atomic force microscopy. *Proceeding of the Conference on Decision and Control, Hawaii*, Dec 2003.
- [17] S. Salapaka, A. Sebastian, J. P. Cleveland, and M. V. Salapaka. High bandwidth nano-positioner: A robust control approach. *Review of Scientific Instruments*, 73(9):3232–3241, September 2002.

- [18] A. Daniele, S. Salapaka, M.V. Salapaka, and M. Dahleh. Piezoelectric Scanners for Atomic Force Microscopes: Design of Lateral Sensors, Identification and Control. In *Proceedings of the American Control Conference, San Diego, California*, pages 253–257, June 1999.
- [19] D. Croft, G. Shedd, and S. Devasia. Creep, Hysteresis and Vibration compensation for Piezoactuators: Atomic Force Microscopy Application. *Proceedings of the American Control Conference, Chicago, Illinois*, pages 2123–2128, June 2000.
- [20] D.R. Sahoo, A. Sebastian, and M.V. Salapaka. Transient Signal based sample-detection in Atomic Force Microscopy. *to appear in American Physics Letters*, 2004.
- [21] M. Napoli, B. Bamieh, and M. Dahleh. Optimal Control of Arrays of Microcantilevers. *Journal of Dynamic Systems Measurement and Control*, 121:686–690, December 1999.
- [22] M. Napoli, B. Bamieh, and K. Turner. Mathematical Modeling, Experimental Validation and Observer Design for a Capacitively Actuated Microcantilever. *Proceedings of the 2003 American Control Conf, Denver*, June 4-6 2003.
- [23] S. Kasas and A. Ikai. A method for anchoring round shaped cells for atomic force microscope imaging. *Biophysical Journal*, 68(5):1678–1680, 1995.
- [24] M. Gad and A. Ikai. Method for immobilizing microbial cells on gel surface for dynamic AFM studies. *Biophysical Journal*, 69(6):2226–2233, 1995.
- [25] Srinivasa M. Salapaka, Tathagata De, and Abu Sebastian. A robust control based solution to the sample-profile estimation problem in fast atomic force microscopy. *International Journal of Robust and Nonlinear Control*, 15(16):821 – 837, 2005. Sample profiles;Fast scan;Set-point regulation;.

- [26] S. Skogestad and I. Postlethwaite. *Multivariable Feedback Control, Analysis and Design*. John Wiley and Sons, 1997.
- [27] G. Schitter, F. Allgower, and A. Stemmer. A new control strategy for high speed atomic force microscopy. *Nanotechnology*, 15(1):108–114, 2004.
- [28] K. Zhou, J.C. Doyle, and K. Glover. *Robust and Optimal Control*. Prentice Hall, Upper Saddle River, NJ 07458, 1996.
- [29] J.C. Doyle, K. Glover, P.P. Khargonekar, and B.A. Francis. State-Space Solutions to Standard h_2 and h_∞ Control Problems. *IEEE Transactions on Automatic Control*, 34(8):831–847, August 1989.
- [30] K. Glover and D. McFarlane. Robust stabilization of normalized coprime factor plant descriptions with \mathcal{H}_∞ -bounded uncertainty. *IEEE transactions on automatic control*, 34(8):821–830, August 1989.
- [31] D. McFarlane and K. Glover. A loop shaping design procedure using \mathcal{H}_∞ synthesis. *IEEE transactions on automatic control*, 37(6):759–769, June 1992.
- [32] J. Sefton and K. Glover. Pole/zero cancellations in the general \mathcal{H}_∞ problem with reference to a two block design. *Systems and Control Letters*, 14(4), 1990.
- [33] A. Sebastian and S. Salapaka. \mathcal{H}_∞ loop shaping design for nano-positioning. In *Proceedings of American Control Conference, Denver*, pages 3708–3713, June 2003.
- [34] N. Ookubo and S. Yumoto. Rapid surface topography using a tapping mode atomic force microscope. *Applied Physics Letters*, 74(15):2149–2151, 1999.

- [35] Tathagata De, Pranav Agarwal, Deepak R. Sahoo, and Murti V. Salapaka. Real-time detection of probe loss in atomic force microscopy. *Applied Physics Letters*, 89(13):133119 –, 2006. Real time signals;Imaging signals;Piezoactuation signals;Reliability index;.
- [36] Constant A. Putman, Kees O. Werf, Bart G. Grooth, Niek F. Hulst, Jan Greve, and Paul K. Hansma. New imaging mode in atomic-force microscopy based on the error signal. *Proceedings of SPIE - The International Society for Optical Engineering*, 1639:198 – 204, 1992.
- [37] T. Sulchek, G.G. Yaralioglu, C.F. Quate, and S.C. Minne. Characterization and optimization of scan speed for tapping-mode atomic force microscopy. *Review of Scientific Instruments*, 73(8):2928 –, 2002.
- [38] Noriyuki Kodera, Hayato Yamashita, and Toshio Ando. Active damping of the scanner for high-speed atomic force microscopy. *Review of Scientific Instruments*, 76(5):053708 –, 2005.
- [39] A.D.L. Humphris, M.J. Miles, and J.K. Hobbs. A mechanical microscope: High-speed atomic force microscopy. *Applied Physics Letters*, 86(3):034106 –, 2005.
- [40] T. Sulchek, R. Hsieh, J.D. Adams, G.G. Yaralioglu, S.C. Minne, C.F. Quate, J.P. Cleveland, A. Atalar, and D.M. Adderton. High-speed tapping mode imaging with active q control for atomic force microscopy. *Applied Physics Letters*, 76(11):1473 – 1475, 2000.
- [41] Tomas R. Rodriguez and Ricardo Garcia. Theory of q control in atomic force microscopy. *Applied Physics Letters*, 82(26):4821 – 4823, 2003.

- [42] M.V. Salapaka, H.S. Bergh, J. Lai, A. Majumdar, and E. McFarland. Multi-mode noise analysis of cantilevers for scanning probe microscopy. *Journal of Applied Physics*, 81(6):2480 –, 1997.
- [43] Nguyen Van. Mitropolsky, IU. A.; Dao. Applied asymptotic methods in nonlinear oscillations. *Dordrecht ; Boston : Kluwer Academic Publishers*, 1997.
- [44] M. Gauthier, N. Sasaki, and M. Tsukada. Dynamics of the cantilever in noncontact dynamic force microscopy: The steady-state approximation and beyond. *Phys. Rev. B*, 64(8):085409, Aug 2001.
- [45] Deepak R. Sahoo, Abu Sebastian, and Murti V. Salapaka. Transient-signal-based sample-detection in atomic force microscopy. *Applied Physics Letters*, 83(26):5521 – 5523, 2003.
- [46] Chris Somerville, Stefan Bauer, Ginger Brininstool, Michelle Facette, Thorsten Hamann, Jennifer Milne, Erin Osborne, Alex Paredez, Staffan Persson, Ted Raab, Sonja Vorwerk, and Heather Youngs. Toward a systems approach to understanding plant cell walls. *Science*, 306(5705):2206 – 2211, 2004. Genetic information;High-resolution imaging;Cell walls;.
- [47] David J. Adams. Fungal cell wall chitinases and glucanases. *Microbiology*, 150(7):2029–2035, 2004.
- [48] John F. Wilkinson Peter Jeffries. Electron microscopy of the cell wall complex of methy-lomonas albus. *Archives of Microbiology*, 119:227–229, 1978-11-01.
- [49] M. Arnoldi, M. Fritz, E. Bäuerlein, M. Radmacher, E. Sackmann, and A. Boulbitch. Bacterial turgor pressure can be measured by atomic force microscopy. *Physical Review E*, 62:1034–1044, July 2000.

- [50] F. Ahimou, F.A. Denis, A. Touhami, and Y.F. Dufrene. Probing microbial cell surface charges by atomic force microscopy. *Langmuir*, 18(18):9937, 2002.
- [51] V. Vadillo-Rodriguez, H.J. Busscher, W. Norde, J. de Vries, and H.C. van der Mei. On relations between microscopic and macroscopic physicochemical properties of bacterial cell surfaces: An afm study on *streptococcus mitis* strains. *Langmuir*, 19(6):2372–2377, 2003.
- [52] Shamik Sen, Shyamsundar Subramanian, and Dennis E. Discher. Indentation and Adhesive Probing of a Cell Membrane with AFM: Theoretical Model and Experiments. *Biophys. J.*, 89(5):3203–3213, 2005.
- [53] AK Adya, E. Canetta, and GM Walker. Atomic force microscopic study of the influence of physical stresses on *Saccharomyces cerevisiae* and *Schizosaccharomyces pombe*. *FEMS Yeast Res*, 2006:120–8, 2001.
- [54] JM Navarro and G. Durand. Modification of yeast metabolism by immobilization onto porous glass. *Applied Microbiology and Biotechnology*, 4(4):243–254, 1977.
- [55] D. McPherson, C. Zhu, Y. Yi, and N. Clark. The Dependency in the Elasticity of the *Saccharomyces cerevisiae* Cell Wall upon Cell Viability and Membrane Integrity. *American Physical Society, APS March Meeting, March 5-9, 2007, abstract# K1. 031*, 2007.
- [56] Tathagata De, Pranav Agarwal, Deepak R. Sahoo, and Murti V. Salapaka. Real-time detection of probe loss in atomic force microscopy. *Virtual Journal of Nanoscale Science & Technology*, 14(15), October 9, 2006.
- [57] Srinivasa Salapaka, Tathagata De, and Abu Sebastian. Sample-profile estimate for fast atomic force microscopy. *Applied Physics Letters*, 87(5):053112 –, 2005. Sample-profile estimates;Sample profiles;Cantilever-tip sample force;Constant tip-sample force;.

- [58] Srinivasa M. Salapaka, De Tathagata, and Abu Sebastian. New approaches for sample-profile estimation for fast atomic force microscopy. *American Society of Mechanical Engineers, Dynamic Systems and Control Division (Publication) DSC*, 74 DSC(2 PART B):1317 – 1326, 2005. Sample-profile estimation;Signal tracks;.
- [59] Deepak R. Sahoo, Tathagata De, and Murti V. Salapaka. Observer based imaging methods for atomic force microscopy. *Proceedings of the 44th IEEE Conference on Decision and Control, and the European Control Conference, CDC-ECC '05*, 2005:1185 – 1190, 2005. Q control method;Active quality factor;Theoretical analysis;Steady state signals;.
- [60] Ralph C. Smith, Andrew G. Hatch, Tathagata De, Murti V. Salapaka, Ricardo C. H. Del Rosario, and Julie K. Raye. Model development for atomic force microscope stage mechanisms. *SIAM Journal on Applied Mathematics*, 66(6):1998 – 2026, 2006. Nanopositioner designs;Nonlinear constitutive relations;Lead zirconate titanate (PZT) devices;.
- [61] Andrew G. Hatch, Ralph C. Smith, Tathagata De, and Murti V. Salapaka. Construction and experimental implementation of a model-based inverse filter to attenuate hysteresis in ferroelectric transducers. *IEEE Transactions on Control Systems Technology*, 14(6):1058 – 1069, 2006. Ferroelectric transducers;Dielectric hysteresis;Inverse filter;.
- [62] Andrew G. Hatch, Ralph C. Smith, and Tathagata De. Experimental implementation of a model-based inverse filter to attenuate hysteresis in an atomic force microscope. *Proceedings of the IEEE Conference on Decision and Control*, 3:3062 – 3067, 2004. Inverse filters;Atomic force microscopes (AFM);Open loop control designs;Control filters;.
- [63] Andrew G. Hatch, Ralph C. Smith, and Tathagata De. Model development and control design for high speed atomic force microscopy. *Proceedings of SPIE - The International*

- Society for Optical Engineering*, 5383:457 – 468, 2004. General densities;Nuclear magnetic resonance microscope (NMRM);Ultra-high resolution;Nanoelectromechanical (NEMS);.
- [64] Ralph C. Smith, Andrew Hatch, and Tathagata De. Model development for piezoceramic nanopositioners. *Proceedings of the IEEE Conference on Decision and Control*, 3:2638 – 2643, 2003. Piezoceramic materials;Nanopositioners;.
- [65] Ralph C. Smith, Murti V. Salapaka, Andrew Hatch, Joshua Smith, and Tathagata De. Model development and inverse compensator design for high speed nanopositioning. *Proceedings of the IEEE Conference on Decision and Control*, 4:3652 – 3657, 2002. Inverse compensator design;Biological processes;.
- [66] H. Sehgal, T. De, S. Nettikadan, and M.V. Salapaka. Micro-manipulation using combined optical tweezers andatomic force microscope. *Proceedings of SPIE*, 6644:66441L, 2007.